Sinking, merging and stationary plumes in a coupled chemotaxis-fluid model: a high-resolution numerical approach

A. Chertock[1], K. Fellner[2]†‡, A. Kurganov[3], A. Lorz[2]§ and P. A. Markowich[2,4,5]

[1] Department of Mathematics, North Carolina State University, Raleigh, NC 27695, USA

[2] Department of Applied Mathematics and Theoretical Physics, Centre for Mathematical Sciences, Wilberforce Road, Cambridge CB3 0WA, UK

[3] Mathematics Department, Tulane University, New Orleans, LA 70118, USA

[4] Department of Mathematics, College of Sciences, King Saud University, Riyadh, KSA

[5] Faculty of Mathematics, University of Vienna, 1090 Wien, Austria

Aquatic bacteria like *Bacillus subtilis* are heavier than water yet they are able to swim up an oxygen gradient and concentrate in a layer below the water surface, which will undergo Rayleigh–Taylor-type instabilities for sufficiently high concentrations. In the literature, a simplified chemotaxis–fluid system has been proposed as a model for bioconvection in modestly diluted cell suspensions. It couples a convective chemotaxis system for the oxygen-consuming and oxytactic bacteria with the incompressible Navier–Stokes equations subject to a gravitational force proportional to the relative surplus of the cell density compared to the water density. In this paper, we derive a high-resolution vorticity-based hybrid finite-volume finite-difference scheme, which allows us to investigate the nonlinear dynamics of a two-dimensional chemotaxis–fluid system with boundary conditions matching an experiment of Hillesdon *et al.* (*Bull. Math. Biol.*, vol. 57, 1995, pp. 299–344). We present selected numerical examples, which illustrate (i) the formation of sinking plumes, (ii) the possible merging of neighbouring plumes and (iii) the convergence towards numerically stable stationary plumes. The examples with stable stationary plumes show how the surface-directed oxytaxis continuously feeds cells into a high-concentration layer near the surface, from where the fluid flow (recurring upwards in the space between the plumes) transports the cells into the plumes, where then gravity makes the cells sink and constitutes the driving force in maintaining the fluid convection and, thus, in shaping the plumes into (numerically) stable stationary states. Our numerical method is fully capable of solving the coupled chemotaxis–fluid system and enabling a full exploration of its dynamics, which cannot be done in a linearised framework.

Key words: bioconvection, computational methods, micro-organism dynamics

---

† Email address for correspondence: Klemens.Fellner@uni-graz.at

‡ Current address: Institute for Mathematics and Scientific Computing, University of Graz, Heinrichstr. 36, 8010 Graz, Austria

§ Current address: Laboratoire Jacques-Louis Lions, Université Pierre et Marie Curie – Paris 6, 4 place Jussieu, 75252 Paris, CEDEX 05, France

1. Introduction

In Hillesdon, Pedley & Kessler (1995), Dombrowski *et al.* (2004) and Tuval *et al.* (2005), several related coupled chemotaxis–fluid model systems have been proposed to describe the collective behaviour of a suspension of oxytactic bacteria in an incompressible fluid under the assumptions that the contribution of bacteria to the bacteria–fluid suspension is sufficiently small (since the density of the bacteria suspension is approximately equal to the density of the fluid) and that more detailed cell–cell interactions (such as hydrodynamic interaction) are neglected. This collective behaviour is also known as bio-convection. In this paper, we study the following system:

$$\left.\begin{aligned}
&n_t + \boldsymbol{u} \cdot \nabla n + \chi \nabla \cdot [nr(c)\nabla c] = D_n \Delta n, \\
&c_t + \boldsymbol{u} \cdot \nabla c = D_c \Delta c - n\kappa r(c), \\
&\rho(\boldsymbol{u}_t + \boldsymbol{u} \cdot \nabla \boldsymbol{u}) + \nabla p = \eta \Delta \boldsymbol{u} - n\nabla \Phi, \\
&\nabla \cdot \boldsymbol{u} = 0,
\end{aligned}\right\} \quad (1.1)$$

where $\Delta := \partial_x^2 + \partial_y^2$ is the Laplacian, n and c are the concentrations of bacteria and oxygen, respectively, κ is the oxygen consumption rate, and $\boldsymbol{u}$ is the velocity field of a fluid flow governed by the incompressible Navier–Stokes equations with density ρ, pressure p and viscosity η. In the fluid equation, $\nabla \Phi := V_b g(\rho_b - \rho)\boldsymbol{z}$ describes the gravitational force exerted by a bacterium onto the fluid along the upwards unit vector $\boldsymbol{z}$ proportional to the volume of the bacterium V_b, the gravitation acceleration $g = 9.8$ m s^{-2}, and the density of bacteria is ρ_b (bacteria are about 10 % denser than water).

In (1.1), both the density of the bacteria n and the oxygen concentration c are convected with the fluid and diffuse with their respective diffusion constants D_n and D_c. The oxygen is consumed proportional to the density of cells n and a dimensionless cut-off function $r(c)$, which models an inactivity threshold of the bacteria due to low oxygen supply. Moreover, in a chemotactic response, the bacteria are directed towards a higher oxygen concentration depending on the chemotactic sensitivity χ and the same cut-off-function $r(c)$. Experiments suggest that the cut-off function can be modelled, for instance, by a step function $r(c) = \theta(c - c^*)$ (see Tuval *et al.* 2005).

Let us emphasise that in contrast to models for chemotactical aggregation like, for example, the well-known Keller–Segel model, the bacteria in (1.1) consume the chemical instead of producing it and the n-term in the c-equation has the opposite sign compared to the Keller–Segel system. Nevertheless, the chemotactic motion of the bacteria introduces a non-local nonlinearity to the system (1.1) and leads to – as our numerical examples will show – more complex dynamics than is observed in a suspension of e.g. sand in water (or inactive, oxygen-starved bacteria) subject to gravity.

For a comprehensive review on bio-convection and the general biological background of systems like (1.1) we refer to Hill & Pedley (2005) and the references therein. The particular model (1.1) was proposed in Hillesdon *et al.* (1995) to describe experiments with a quasi-two-dimensional suspension of the swimming bacteria *Bacillus subtilis* in a thin chamber of water (see figure 1). In these experiments the bacteria consume oxygen, which diffuses through the water surface into the water. Thus, an initially stirred, quasi-homogeneous suspension of bacteria will swim up the oxygen gradient, which lets some bacteria concentrate below the surface, while other bacteria are rendered inactive wherever the oxygen concentration has fallen below the threshold of activity. Later on, Rayleigh–Taylor-type instabilities appear in
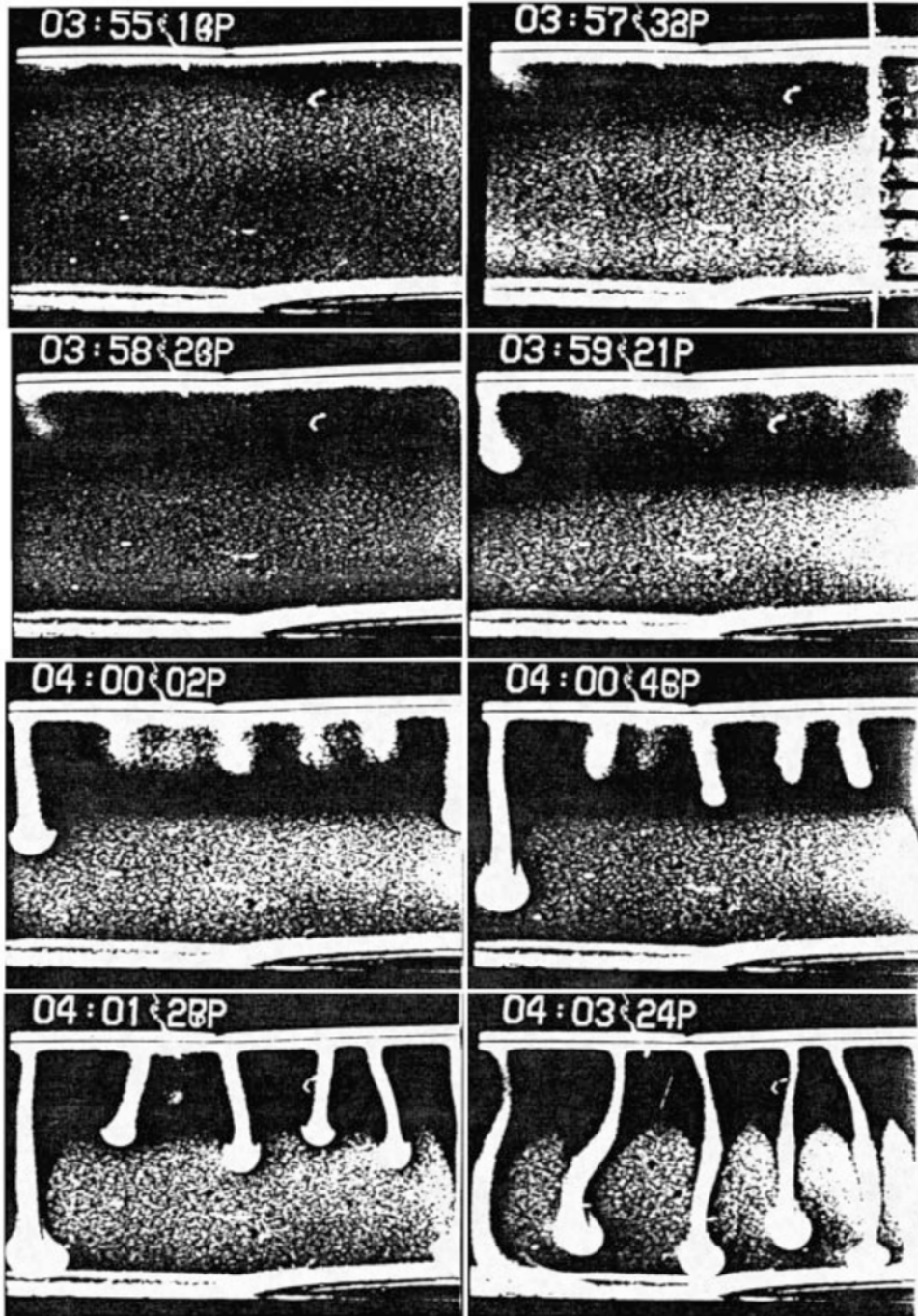
FIGURE 1. Snapshots of a suspension of the aerobic bacteria *B. subtilis* reproduced with kind permission from Hillesdon *et al.* (1995). The initial suspension is well stirred and quasi-homogeneous. First, a high-concentration layer forms near the surface as cell swim up following the oxygen gradient. Later, instabilities form at this layer and finger-shaped plumes begin to sink downwards, which turn into mushroom-shaped plumes in the areas where the oxygen concentration is below the chemotaxis threshold $r(c)$.

a sufficiently concentrated cell layer near the surface as the bacteria are about 10 % denser than water. These instabilities will develop further into plumes of cells sinking downwards. We refer to Hillesdon & Pedley (1996) for the linear stability analysis of the system (1.1), while weakly nonlinear stability was discussed in Metcalfe & Pedley (1998).

A first local existence result for (1.1) and related systems was obtained in Lorz (2010). Global existence was shown in Duan, Lorz & Markowich (2010) for small initial concentrations of the oxygen c and without the convection term in the u-equation, that is, for the Stokes equation instead of the Navier–Stokes equation, which is a reasonable simplification for the expected low-Reynolds-number flow. For a single *Bacillus subtilis* the Reynolds number is of order 10^{-4} while in bio-convective vortices Reynolds numbers of order 10^{-2} are observed, see e.g. Wolgemuth (2008) and Tuval *et al.* (2005). Global existence of a model with nonlinear cell diffusion in the n-equation was investigated in Di Francesco, Lorz & Markowich (2010).

In this paper, we present a high-resolution numerical scheme in order to study the nonlinear dynamics of solutions of the model (1.1) in a rectangular two-dimensional (2-D) domain. Matching the experiment depicted in figure 1, we shall consider the following *mixed boundary conditions*: the boundary condition at the top $\partial\Omega_{top}$ describes the fluid–air surface, where there is no cell flux, the oxygen will be saturated with the air oxygen concentration c_{air} and the vertical fluid velocity and the tangential fluid stress are assumed zero (see e.g. Hillesdon & Pedley 1996; Metcalfe & Pedley 1998, 2001; Tuval *et al.* 2005):

$$\chi n r(c) c_y - D_n n_y = 0, \quad c = c_{air}, \quad v = 0, \quad u_y = 0, \quad \forall (x, y) \in \partial\Omega_{top}, \qquad (1.2)$$

where u and v are the horizontal and vertical components of the velocity vector $\mathbf{u}$, respectively. At the bottom of the domain $\partial\Omega_{bot}$, the cell and oxygen fluxes and the fluid velocity are supposed zero:

$$n_y = c_y = 0, \quad u = v = 0, \quad \forall (x, y) \in \partial\Omega_{bot}. \qquad (1.3)$$

Finally, periodic boundary conditions at the left and right sides of the domain are imposed in order to avoid any impact of these boundaries.

Previously, Hopkins & Fauci (2002) used a particle method modelling the bacteria as an ensemble of discrete balls which was coupled to a finite-volume method for the equation for the chemical and for the Navier–Stokes equations (see also Saintillan & Shelley 2007 for bacteria modelled as rods). Moreover, Ghorai & Hill (1999, 2002) calculated a suspension of swimming, gyrotactic micro-organism in tall, narrow 2-D chambers using a conservative finite-difference scheme. Furthermore, in Hernandez-Ortiz, Underhill & Graham (2009) simulation studies have been performed using particle-based methods on bacterial suspensions in confined geometries.

Here, we develop a high-resolution hybrid finite-volume finite-difference method for the numerical solution of the coupled chemotaxis-fluid system (1.1). The main advantage of our approach is that it allows us to take advantage of two different methods applied to two different parts (chemotaxis and fluid) of the studied system. The chemotaxis equations are discretised using a semi-discrete second-order finite-volume upwind scheme. In general upwind schemes are commonly used numerical methods for convection–diffusion equations in the case of a convection-dominated regime, see e.g. LeVeque (2002) and references therein. When the physical viscosity is low the numerical solution is stabilised via numerical diffusion, which (especially for second- and higher-order upwind schemes) rapidly vanishes as the mesh size goes to zero so that a high resolution is achieved. Another important property

satisfied by our upwind scheme is its ability to preserves the positivity of the computed cell density. As it was demonstrated in Chertock & Kurganov (2008) this property enforces nonlinear stability which is crucial for the computed solutions of the chemotaxis equations to remain non-oscillatory. The second part of the system – the incompressible Navier–Stokes equations – is first rewritten in the vorticity formulation and then numerically solved by a semi-discrete second-order finite-difference method applied to the non-conservative transport form of the vorticity equation. This choice is motivated by the fact that the Reynolds numbers under consideration are relatively small and hence the amount of physical diffusion present in the fluid part of the system is sufficiently large to stabilise a highly accurate and simple central-difference scheme. Therefore, no upwinding is needed for the fluid equation.

Our hybrid finite-volume finite-difference method is semi-discrete and the resulting system of time-dependent ordinary differential equations (ODEs) must be integrated using an appropriate ODE solver. Since the efficiency of the obtained fully discrete scheme obtained depends on the efficiency of the ODE solver, one may want to select either an implicit or implicit–explicit (IMEX) method, which may typically be utilised with large time steps. These methods, however, require solving large systems of (linear) algebraic equations which may substantially reduce the efficiency of the method. We prefer an alternative approach: we use an explicit large-stability-domain third-order Runge–Kutta method from Medovikov (1998*a,b*) which typically outperforms implicit methods in solving ODE systems obtained after semi-discretisations of convection–diffusion equations.

Using the high-resolution numerical scheme developed, we perform several numerical experiments reported in §3. Our main goal is to study the nonlinear dynamics of (1.1) and to understand the interplay of gravity and chemotaxis in the formation of plumes, as well as their surrounding fluid convection. In particular, in §4, we observe the formation of sinking plumes out of randomly perturbed homogeneous initial data. Moreover, these plumes merge depending on the spacing set by the random initial data, which is reminiscent of merging Rayleigh–Bénard-type patterns. A second example in §5 shows the convergence towards numerically stable stationary plumes and how the surrounding fluid convection is responsible for maintaining the shape of the plumes. In §6, an example quite similar to figure 1 demonstrates that the chemotactic motion in (1.1) is, ultimately, responsible for the maintenance of the fluid convection, and thus, for the shape of plumes at large times. In §7, this is further detailed in an additional example.

The novelty of this paper is that for the first time a numerical scheme has been able to fully capture and explore the nonlinear dynamics described by (1.1). Compared to Hopkins & Fauci (2002) we explore the chemotactic effects in much greater depth. Moreover unlike Metcalfe & Pedley (1998, 2001) we do not need to consider linearisation techniques which neglect higher-order terms and make it impossible to study fully nonlinear effects.

As a next step it would be interesting to investigate the effects of droplet geometry (curvature of the upper part of the boundary of the simulation domain) and the effect of a third spatial dimension. However, this will be subject of a forthcoming paper.

This paper is organised as follows. First, in §2, we perform the non-dimensionalisation of the system studied (1.1) and recall the vorticity formulation of the incompressible Navier–Stokes equations. We derive a numerical method by implementing the semi-discrete second-order hybrid finite-volume finite-difference scheme, which is described in detail in appendix A. The accuracy of the scheme is verified at the beginning of §3 by comparing an analytical steady-state solution

with the numerical one. Moreover, in § 3 we show that the numerical scheme is able to reproduce an example of bifurcation of the stationary state as predicted by the linear stability analysis in Hillesdon & Pedley (1996). Finally, we present numerical examples showing the formation and the merging of plumes out of random initial data (§ 4) and the convergence towards stationary plumes in the absence of oxygen cut-off (i.e. c remains larger than $c^* = 0.3$, see § 5) and in presence of oxygen cut-off (§§ 6 and 7).

2. Scaling and set-up for numerics

We denote by L a characteristic length (we may choose, for instance, L to be the height of the water chamber in figure 1) and the characteristic cell density by n_r. Rescaling the variables according to Tuval *et al.* (2005) as follows:

$$x' = \frac{x}{L}, \quad t' = \frac{D_n}{L^2}t, \quad c' = \frac{c}{c_{air}}, \quad n' = \frac{n}{n_r}, \quad p' = \frac{L^2}{\eta D_n}p, \quad u' = \frac{L}{D_n}u, \quad (2.1)$$

leads to the five dimensionless parameters α, β, γ, δ and the Schmidt number Sc, which characterise the system (1.1):

$$\alpha := \frac{\chi c_{air}}{D_n}, \quad \beta := \frac{\kappa n_r L^2}{c_{air} D_n}, \quad \gamma := \frac{V_b n_r g(\rho_b - \rho)L^3}{\eta D_n}, \quad \delta := \frac{D_c}{D_n}, \quad Sc := \frac{\eta}{D_n \rho}, (2.2)$$

where c_{air} is the oxygen concentration of the air above the fluid. Note that the parameters α and β differ slightly from e.g. Hillesdon & Pedley (1996) and Metcalfe & Pedley (1998). Three of these parameters, namely α, δ and Sc, are set by the properties of bacteria, fluid and air. Typical values for *Bacillus subtilis* in water are $\alpha = 10$, $\delta = 5$ and $Sc = 500$ (see e.g. Tuval *et al.* 2005). The remaining two parameters β and γ depend also on the chosen length scale L and, in particular, on the reference cell density n_r and will thus be varied in the numerical examples in § 3.

After dropping the prime notation in the rescaled variables, we rewrite the fluid equations in the vorticity formulation: with $\boldsymbol{x} = (x, y)^T$ and $\boldsymbol{u} = (u, v)^T$ we introduce the vorticity by $\omega := v_x - u_y$ and the stream-function ψ such that $u = \psi_y$ and $v = -\psi_x$ to obtain the following system:

$$n_t + \nabla \cdot (\boldsymbol{u}n) + \alpha \nabla \cdot [r(c)n\nabla c] = \Delta n, \quad (2.3)$$
$$c_t + \nabla \cdot (\boldsymbol{u}c) = \delta \Delta c - \beta r(c)n, \quad (2.4)$$
$$\omega_t + \nabla \cdot (\boldsymbol{u}\omega) = Sc \, \Delta\omega - \gamma \, Sc \, n_x, \quad (2.5)$$
$$\Delta\psi = -\omega. \quad (2.6)$$

The resulting system (2.3)–(2.6) is considered on a rectangular domain $\Omega = [-a, a] \times [0, d]$ subject to the initial data

$$n(x, y, t = 0) = n_0(x, y), \quad c(x, y, t = 0) = c_0(x, y), \quad \boldsymbol{u}(x, y, t = 0) = \boldsymbol{u}_0(x, y), \quad (2.7)$$

and the following boundary conditions: at the top and the bottom of Ω we set

$$\alpha r(c)nc_y - n_y = 0, \quad c = 1, \quad v = 0, \quad u_y = 0, \quad \forall(x, y) : y = d, \quad (2.8)$$
$$n_y = c_y = 0, \quad u = v = 0, \quad \forall(x, y) : y = 0, \quad (2.9)$$

while at the sides of Ω (that is, at $x = \pm a$) the boundary conditions are periodic. Alternatively, the above boundary conditions can be written in terms of the vorticity

and stream-function as follows:

$$\alpha r(c)nc_y - n_y = 0, \quad c = 1, \quad \omega = 0, \quad \psi = 0, \quad \forall(x, y) : y = d, \qquad (2.10)$$

$$n_y = c_y = 0, \quad \psi_y = 0, \quad \omega = -\psi_{yy}, \quad \forall(x, y) : y = 0. \qquad (2.11)$$

Note that the Poisson equation implies $\psi_{xx} = 0$ at the lower boundary $y = 0$, which together with the periodicity and continuity gives $\psi = \text{const}$ at $y = 0$. Thus, $v = 0$ at $y = 0$ follows.

3. Discussion of the numerical examples

In the following sections we present selected numerical experiments with the system (2.3)–(2.6) on the rectangular domain (typically $\Omega = [-3, 3] \times [0, 1]$ except in figure 3) subject to the boundary conditions (2.10) and (2.11). The results are obtained using a hybrid finite-volume finite-difference scheme, described in detail in appendix A.

In these examples (again except in figure 3), we set the coefficients α, δ and the Schmidt number Sc to model a suspension of swimming bacteria, for example, *Bacillus subtilis* in water (see e.g. Tuval *et al.* 2005):

$$\alpha = 10, \quad \delta = 5, \quad Sc = 500, \qquad (3.1)$$

and take the cut-off function $r(c)$, which modulates the oxygen consumption rate, to be

$$r(c) = \begin{cases} 1 & \text{if } c \geqslant 0.3, \\ 0 & \text{if } c < 0.3. \end{cases} \qquad (3.2)$$

The numerical examples will vary the initial data and the two remaining parameters $\beta = (\kappa n_r L^2)/(c_s D_n)$ and $\gamma = (V_b n_r g(\rho_b - \rho)L^3)/(\eta D_n)$ (see (2.2)), in particular, by choosing different reference values of the bacteria concentration n_r, which is proportional to both β and γ.

The numerical simulations were performed using the numerical method described in appendix A on uniform grids. Mesh refinement convergence tests have been successfully performed to check the numerical convergence of the developed method (see § 5), but they will not be reported here. We only show the results obtained on the grid with $\Delta x = \Delta y = 0.02$.

The time integration of (A 10), (A 34) should be performed using an efficient, stable and sufficiently accurate numerical method. Since the studied system is parabolic-elliptic, one may want to use an implicit ODE solver, which requires a computationally expensive linear algebra solver, but in general does not have any stability restriction on the size of time steps. We follow an alternative approach and integrate the ODE system (A 10), (A 34) using DUMKA3 – the explicit third-order large-stability-domain Runge–Kutta method, developed in Medovikov (1998*b*) (see also Medovikov 1998*a*). This high-order integration produces accurate results, and its larger stability domains (in comparison with the standard explicit Runge–Kutta methods) allow one to use bigger time steps; the explicit form retains simplicity, and the embedded formulae permit an efficient step size control. In practice these methods preserve all the advantages of explicit methods and work as fast as implicit methods (see Medovikov 1998*b*, for details).

It should be observed, however, that, unlike the strong stability-preserving (SSP) Runge–Kutta or IMEX-SSP methods, this method is not a positivity-preserving ODE solver. In our numerical experiments, we did not observe negative cell density values, but they, in principle, may appear. In the latter case, the efficient DUMKA3 solver

should be used from the beginning. If after a certain time step, a negative value of the computed cell or oxygen density emerges, this step should be rejected and an SSP time step should be performed instead. Then, one has to switch back to the DUMKA3 solver.

3.1. *Comparison of numerical and analytical steady-state solutions*

It is known from Hillesdon *et al.* (1995) that for suitable parameters (for instance, for sufficiently low initial cell densities) solutions of (2.3)–(2.6) converge to homogeneous-in-x steady-state solutions of the following time-independent system:

$$\alpha \nabla \cdot [r(c)n\nabla c] = \Delta n, \quad 0 = \delta \Delta c - n\beta r(c). \tag{3.3}$$

Thus, a natural test of the numerical scheme compares analytic homogeneous-in-x stationary solutions, which can be explicitly computed provided that $c \geqslant 0.3$ and, thus, $r(c) = 1$ in the entire domain (see e.g. Hillesdon *et al.* 1995), with numerically computed stationary solutions.

For the sake of clarity, we re-sketch the derivation of homogeneous-in-x steady-state solutions. For $n(x, y)$ and $c(x, y)$ solutions of (3.3), we set $n^s(y) = n(x, y)$ and $c^s(y) = c(x, y)$ (independent of x) and obtain

$$\alpha \left[n^s c_y^s \right]_y = n_{yy}^s, \quad \delta c_{yy}^s = n^s \beta. \tag{3.4}$$

Integrating (3.4) and recalling the boundary conditions yields firstly

$$\alpha n^s c_y^s = n_y^s \tag{3.5}$$

and

$$c_y^s(1) = \frac{\beta}{\delta} \int_0^1 n^s \, \mathrm{d}y, \tag{3.6}$$

and secondly using (3.4)

$$\delta c_{yyy}^s = n_y^s \beta = \alpha \beta n^s c_y^s = \alpha \delta c_{yy}^s c_y^s \implies c_{yy}^s = \frac{\alpha}{2}((c_y^s)^2 + A), \tag{3.7}$$

where A is a constant. Further integration shows that in order to satisfy (3.6), A has to be positive. Finally, it follows from (3.5) that

$$c^s(y) = 1 - \frac{2}{\alpha} \ln \left(\frac{\cos \left(\frac{\alpha}{2} Ay \right)}{\cos \left(\frac{\alpha}{2} A \right)} \right), \quad n^s(y) = \frac{\delta A^2}{\beta} \frac{\alpha}{2} \frac{1}{\cos^2 \left(\frac{\alpha}{2} Ay \right)}. \tag{3.8}$$

We now numerically solve the system (2.3)–(2.6) with the boundary conditions (2.10), (2.11), $\beta = 10$, $\gamma = 10^3$, and the rest of the parameters specified in (3.1). The constant initial data are

$$n_0(x, y) = \frac{\pi}{40}, \quad c_0(x, y) = 1, \quad \boldsymbol{u}_0(x, y) = \boldsymbol{0}. \tag{3.9}$$

We take $A = \pi/20$, which satisfies the relationship (see (3.6) and (3.8)):

$$\beta \int_0^1 n^s(y) \, \mathrm{d}y = \delta A \tan \left(\frac{\alpha}{2} A \right) = \beta \frac{\pi}{40} = \frac{\pi}{4}. \tag{3.10}$$

We run the code until the numerical solution converges to its steady state and compute the obtained results with the analytical solution (3.8), for which it is easy to verify
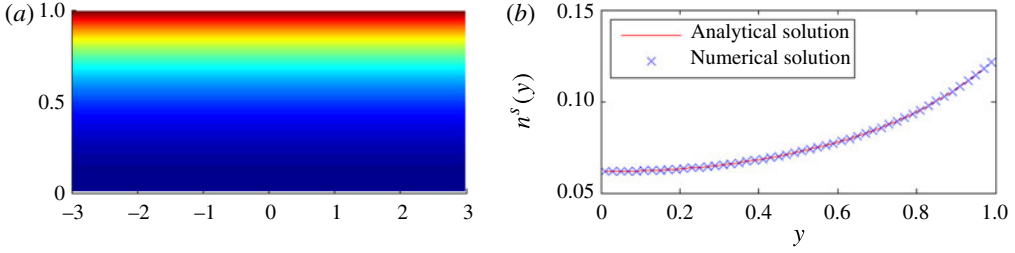
FIGURE 2. The n-component of the numerical steady-state solution (a) and the agreement of its vertical profile with the analytically calculated one (b).

that $c^s(y) > 0.3$ and thus $r(c) \equiv 1$. As one can see in figure 2, the numerical and analytical solutions are in a very good agreement.

3.2. *Comparison of numerics and linear stability analysis: the onset of convection pattern*

As a second test of the numerical scheme, we consider an example presented in Hillesdon & Pedley (1996), where the linear stability analysis of (2.3)–(2.6) (with the cut-off $r(c)$ being also applied to the cell diffusion in (2.3)) predicts for the parameters $\alpha = 5$, $\delta = 0.2$, $\beta = 4$, $\gamma = 418$ and $Sc = 7700$ the loss of stability of the homogeneous-in-x steady state and the onset of convection pattern with a critical wavenumber $k_c \approx 2.53$, i.e. with wavelength $\lambda_c = 2\pi/k_c \approx 2.48$ (Hillesdon & Pedley 1996, figure 16). We thus choose $a = 2.48$ and $\Omega = [-2.48, 2.48] \times [0, 1]$ in order to allow the periodic boundary conditions to capture possible convection patterns with this wavelength.

We take $r(c)$ given by (3.2) and the following initial conditions:

$$n_0(x, y) = \begin{cases} 1, & y > 0.501 - 0.01 \cos(2\pi x/2.483), \\ 0.5, & \text{otherwise}, \end{cases} \quad c_0(x, y) = 1, \boldsymbol{u}_0(x, y) = \boldsymbol{0},$$

(3.11)

which prescribes small, sinusodial modulations of the lower edge of an upper layer with cell concentration higher than at the bottom. Such *plume-precursors* should trigger the onset of plumes *independently from the numerical precision*.

Figure 3(a) shows the computed quasi-homogeneous-in-x cell density n at time $t = 0.8$. The corresponding vertical n and c profiles as plotted in figure 3(b) compare very well with figure 14 in Hillesdon & Pedley (1996) (reproduced in figure 3e) once taking into account that figure 3(e) plots $\delta = 1/4$ instead of $\delta = 0.2$ (please note the difference in the definition of parameters compared to Hillesdon & Pedley 1996, i.e. $\alpha \rightarrow \gamma_{HP}$, $\beta/\delta \rightarrow \beta_{HP}$, $\gamma \rightarrow \Gamma_{HP}$). Note, that the vertical cell-density profile (blue line) shows clearly an increase of cells towards the bottom, which is due to the cut-off of the chemotactic convection for oxygen levels (red line) below $c \leqslant 0.3$. Moreover, the predicted onsetting convection pattern is correctly captured by the numerical stream-function and velocity field (the latter is only plotted for the left half of the domain), shown in figure 3(c). In figure 3(d) we reproduce figure 16 of Hillesdon & Pedley (1996), which predicts the stationary stream-function for exactly the above parameters including $\delta = 0.2$.
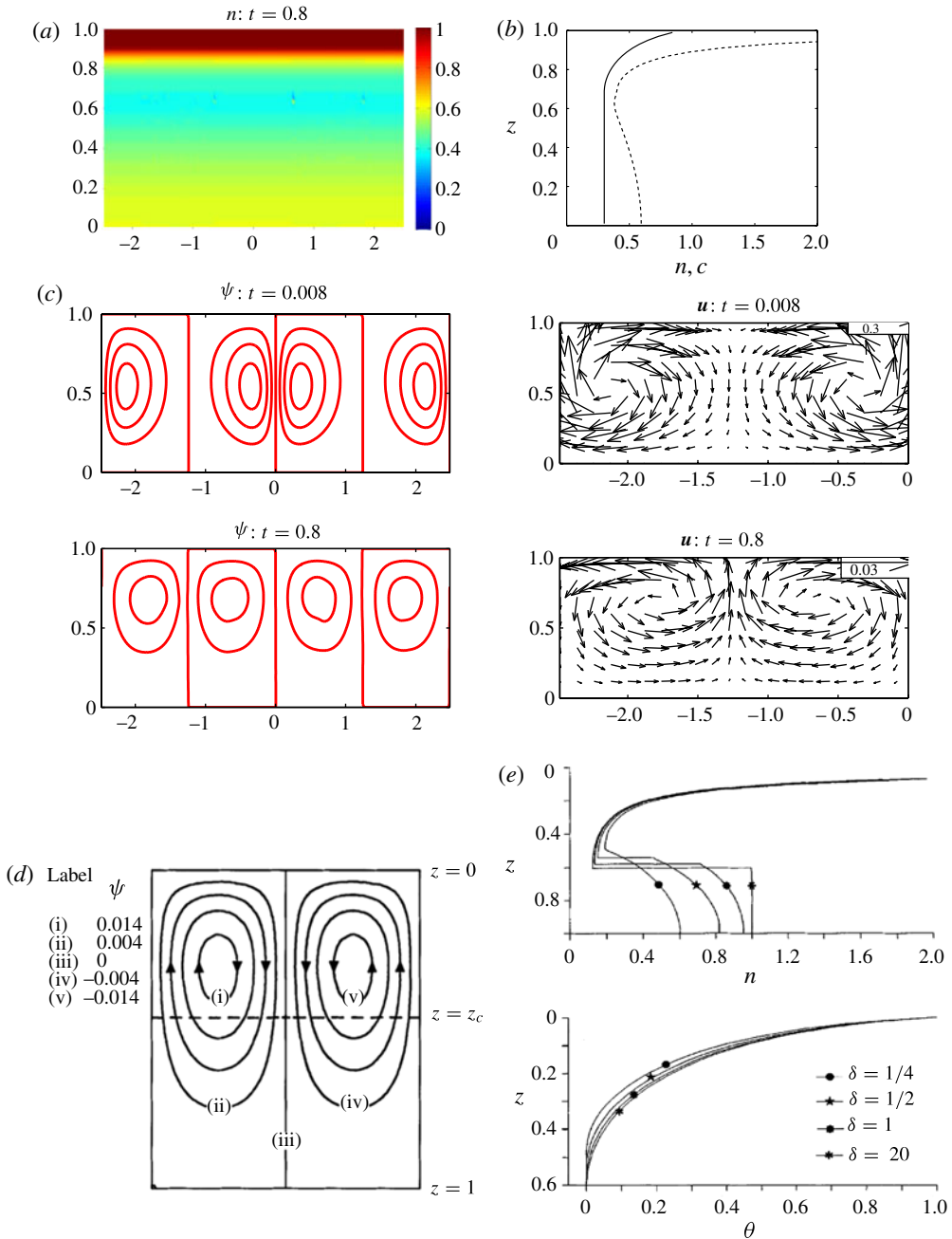
FIGURE 3. (Colour online available at journals.cambridge.org/flm) Comparison with linear stability analysis and the onset of convection pattern in Hillesdon & Pedley (1996, figures 14 and 16): numerical solution of (2.3)–(2.6) with $\alpha = 5$, $\delta = 0.2$, $\beta = 4$, $\gamma = 418$ and $Sc = 7700$ yielding a critical wavenumber $k_c \approx 2.53$ and wavelength $\lambda_c \approx 2.48$. (*a*) Cell density n at time $t = 0.8$; (*b*) vertical profiles of the cell density n (dashed) and the oxygen densities c (bold) at time $t = 0.8$. (*c*) Stream-function and fluid velocity (the latter is shown in the left half of the domain) at times $t = 0.08$, $t = 0.8$. (*d*) Stream-function plot from Hillesdon & Pedley (1996, figure 16) for these parameters. (*e*) Plots from Hillesdon & Pedley (1996, figure 14) for the oxygen concentration θ (lower plot) and the cell density n (upper plot) for $\delta = 1/4$ instead of $\delta = 0.2$.

4. Plume formation and merging plumes: randomly perturbed homogeneous initial data

As mentioned above, following the linear stability analysis of Hillesdon & Pedley (1996), it is expected that the homogeneous-in-x steady-state solutions for the system (2.3)–(2.6) as depicted in figure 2 are unstable for certain parameters. In particular, for a sufficiently high reference density of cells n_r and, thus, for sufficiently large β and γ, Rayleigh–Taylor instabilities of a layer with high cell concentration near the surface (see, e.g. Chandrasekhar 1981; Sharp 1984) will cause plume-like structure and convection cells to appear.

The numerical simulation of these instabilities is highly non-trivial (see e.g. Sharp 1984; Cook & Dimotaki 2001). However, the examples in this and the following sections demonstrate that our numerical scheme succeeds in resolving large-scale plume structures (as shown in figure 1) for a wide range of system parameters, in particular for the bacteria-typical choices of α, δ and Sc in (3.1).

4.1. *Parameters and initial data*

As a first example case, we shall study the solution of the system (2.3)–(2.6) with the boundary conditions (2.10), (2.11) and the bacteria-typical parameters (3.1) and with $\beta = 20$ and $\gamma = 2 \times 10^3$, which corresponds to a doubled reference density of cells n_r (recall from § 2 that $\beta \propto n_r$ and $\gamma \propto n_r$) compared to figure 2 (homogeneous stationary state). Moreover, as initial data, we consider homogeneous initial data with a random perturbation in the cell concentration:

$$n_0(x, y) = 0.8 + 0.2\xi, \quad c_0(x, y) = 1, \quad \boldsymbol{u}_0(x, y) = \boldsymbol{0}, \tag{4.1}$$

where ξ is a random variable uniformly distributed in the interval [0, 1]. Note that the above randomly perturbed initial data (4.1) do not introduce a new length scale besides the periodicity of the domain.

4.2. *Time evolution: plume formation and merging of plumes*

Figure 4 shows the time evolution of the n (cells) and c (oxygen) components of the computed solution. Due to the larger amount of cells compared to figure 2, we observe already at time $t = 0.16$ several instabilities at the lower edge of a layer of high cell concentration below the air–fluid surface, which has formed as a majority of bacteria swam up the oxygen gradient. At $t = 0.32$, these instabilities, amplifying the random irregularities of the initial data, developed into four falling plumes. Moreover by this time the oxygen concentration c in most of the bottom half of the domain has dropped below the chemotaxis cut-off ($c < 0.3$ and thus $r(c) = 0$ there) due to the amount of bacteria present there. Thus, the bacteria in this region become inactive and stop directed swimming yet they continue (along with the fluid) to sink down into the bottom part of the domain.

We remark that figure 4 shows that – perhaps somewhat counterintuitively – the cell diffusion is a prominent effect wherever the bacteria are chemotactically inactive. In fact, one might consider (as it was done in Hillesdon & Pedley 1996, for instance) a model where diffusion is cut off with $r(c) = 0$ along with the chemotaxis. In the present paper however, we refrained from doing so and are interested in allowing figure 4 to show how strongly constant cell diffusion needs to be counteracted by the effects of the fluid convection and the chemotaxis for the plumes to remain so sharply profiled as they are in the upper halves of figure 4. Moreover, we conjecture that a diffusion cut-off with $r(c)$ would not significantly influence the formation of plumes *per se* since the plume formation happens essentially in this upper half where the
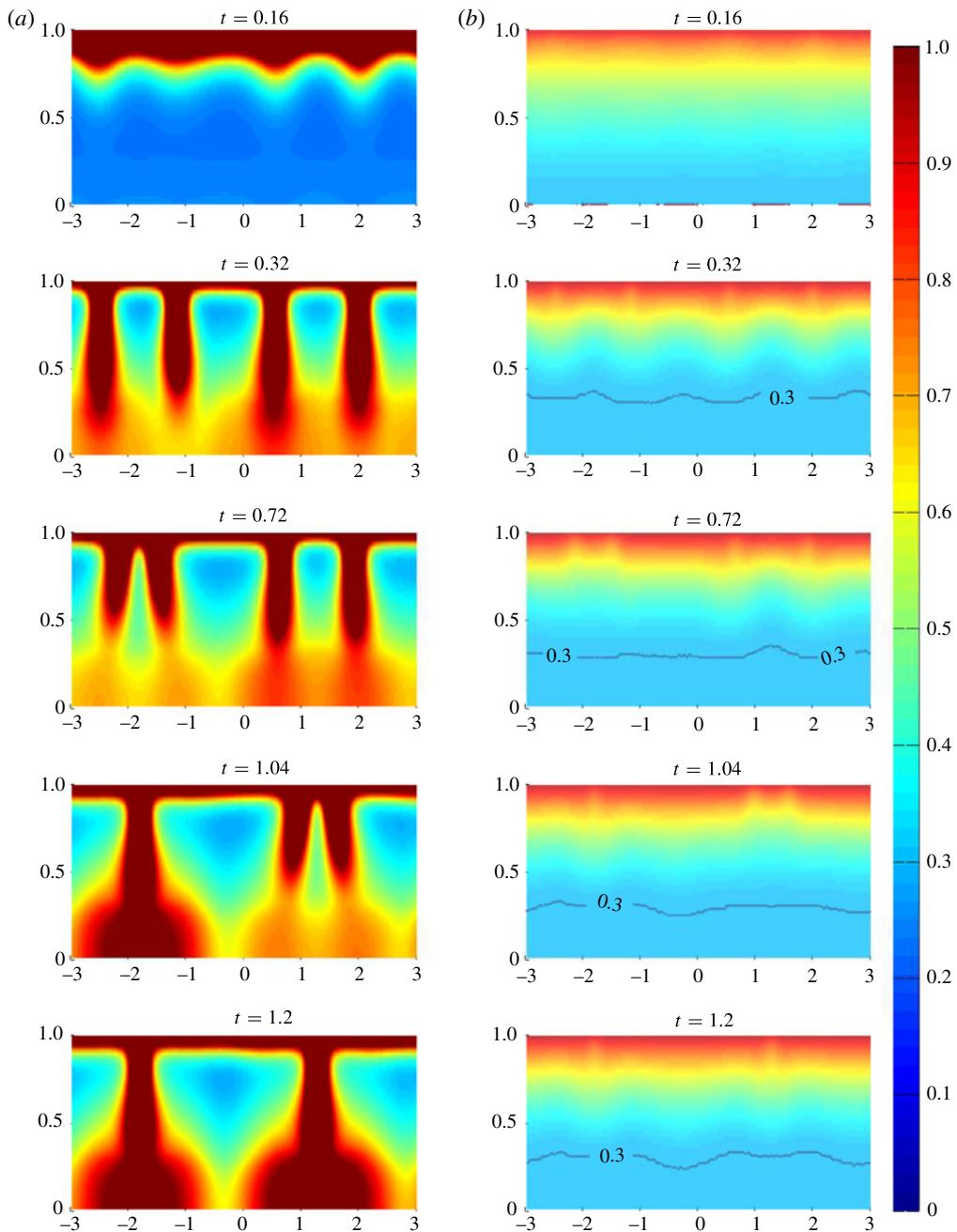
FIGURE 4. (*a*) Cell density *n* and (*b*) oxygen concentration *c* of the computed solution of (2.3)–(2.6) with randomly perturbed homogeneous initial data (4.1) and parameters (3.1) and $\beta = 20$ and $\gamma = 2 \times 10^3$. At time $t = 0.16$, we observe instabilities at the lower edge of a high-concentration layer near the oxygen-rich surface. At $t = 0.32$ four falling plumes have formed, which start merging later ($t = 0.72$), first into three ($t = 1.04$) and finally into two plumes ($t = 1.2$). To highlight and colour the plumes in the best way, all large values of $n \geqslant 1$ near the surface are drawn equally red.
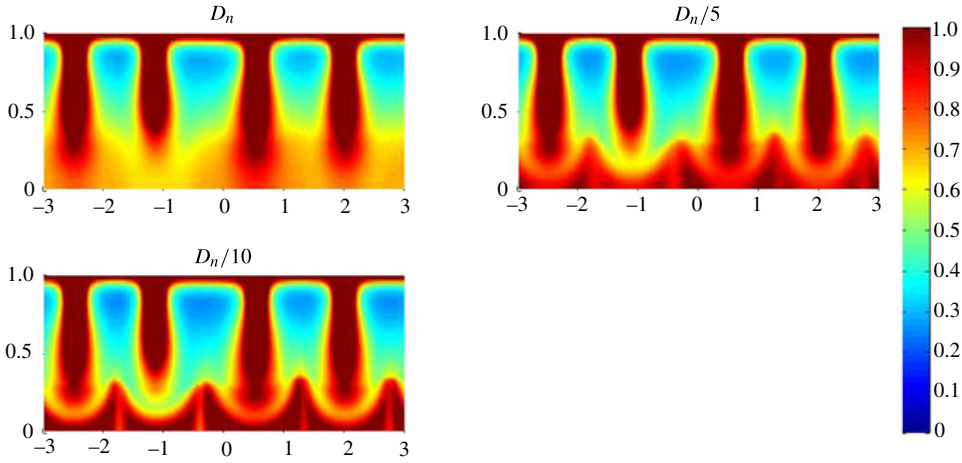
FIGURE 5. Comparison of cell density n of the computed solution of (2.3)–(2.6) with randomly perturbed homogeneous initial data (4.1) at time $t = 0.32$ for oxygen cut-off $c < 0.3$ leading to a decrease cell diffusion $\delta = 5$ (a, no decrease in D_n), $\delta = 25$ (b, decreased D_n by factor 5) and $\delta = 50$ (c, decreased D_n by factor 10). The remaining parameters are $\alpha = 10$, $Sc = 500$, $\beta = 20$ and $\gamma = 2 \times 10^3$. To highlight and colour the plumes in the best way, all large values of $n \geqslant 1$ near the surface are drawn equally red.

chemotaxis is active. Finally, we have observed that preliminary numerical simulations with diffusion cut-off show small-structured, unrealistic convection patterns in areas with diffusion cut-off, which we thus believe not to be a good model for describing the biological experiment in figure 1. Numerical simulation of a modified model, where the cell diffusion is not turned off but continuously tuned down (to the effects of the Brownian motion of the fluid), along with the chemotaxis cut-off are the subject for a forthcoming paper discussing several model variations of (2.3)–(2.6).

Later at time $t = 0.72$ in the time evolution, we observe that the left two plumes are approaching each other and merge into a large plume at time $t = 1.04$. With the bacteria competing for oxygen, the merging of plumes can hardly be a chemotaxis effect, which would make the plumes, rather, repel each other. Therefore, the merging of plumes must be a fluid-dynamic effect similar to the merging of Rayleigh–Bénard convection cells (see e.g. Chapman & Proctor 1980; Busse 1985; Busse & Sieber 1991).

However, the fact that plumes merge shows also that the initially formed number of plumes is not sustainable on larger time scales. This is a commonly observed feature in many non-local interaction equations like, for instance, in the Keller–Segel aggregation model or in models describing the swarming/flocking of individuals. In these models, the collective behaviour of individuals/particles is given by the action of an inter-particle potential (modelling e.g. the attractive chemotaxis or the repulsive–aggregating interaction of a Morse-type swarming potential) and initially formed aggregates are observed to merge until a stable stationary configuration is reached (see e.g. Dolak & Schmeiser 2005; Fellner & Raoul 2010). The merging of plumes in figure 4 shows that the non-local, nonlinear coupling of fluid and cell motions is equally able to create this behaviour. In figure 4, no further merging of the two remaining plumes is observed after time $t = 1.2$. We ran the computation till $t = 4$. The patterns observed at $t = 1.2$ seem to be stationary.

4.3. *Oxygen cut-off and decreased cell diffusion*

We have also performed tests with a modified version of model (2.3)–(2.6) where the oxygen cut-off threshold $c^* = 0.3$ not only stops the chemotaxis but also decreases the cell-diffusion coefficients D_n. In figure 5 we replot the numerical experiment figure 4 at time $t = 0.32$ without decreased cell diffusion and compare it with the plots with D_n decreased by the factors 5 and 10.

A general comparison with figure 4 shows that the time evolution for decreased cell diffusion leads to the same formation and merging of the plumes. The most significant difference concerns the cell-density profiles in the areas with cut-off. In figure 5 the two plots with decreased cell diffusion, (*b*) and (*c*), show bowl-shaped plume structures at the bottom under a falling plume. The profiles of these standing plumes appear shaped by the recurrent fluid flow and sharpened as the diffusion coefficient is decreased and the fluid convection becomes increasingly dominant. The experimental bacteria suspension in the last picture of figure 1 seems to show similar structures with inactive bacteria at the bottom being shaped into piles between the plumes despite the impression that parameter values and the amount of cells are not well matched between figures 1 and 5.

5. Numerically nonlinearly stable stationary plumes for low-density initial data

In §4, we used the randomly perturbed homogeneous initial data (4.1) as a natural choice in order to simulate experiments like figure 1. While the randomly perturbed homogeneous initial data have the advantage of not prescribing any internal length scale, they are however ill-suited for performing a mesh refinement or other detailed studies of the formation of plumes simply because the random effect prevents a detailed comparison of the computed results. In this section, we study the time evolution of solutions of (2.3)–(2.11) from purely *deterministic initial data* towards a stationary state of plumes in the absence of oxygen cut-off (in Hillesdon & Pedley 1996, this case was referred to as the shallow-chamber case).

5.1. *Parameters and initial data*

We choose the same parameters $\beta = 10$, $\gamma = 10^3$ and (3.1) as for the homogeneous stationary state depicted in figure 2. We also take the following deterministic initial data:

$$n_0(x, y) = \begin{cases} 1 & \text{if } y > 0.499 - 0.01 \sin((x - 1.5)\pi), \\ 0.5 & \text{otherwise,} \end{cases} \qquad c_0(x, y) = 1, \, \boldsymbol{u}_0(x, y) = \boldsymbol{0}.$$

$$(5.1)$$

It should be observed that the total amount of bacteria cells is now ~ 10 times higher than in the initial data (3.9) used in figure 2.

5.2. *Time evolution: formation of stationary plumes*

In figure 6, we show the time evolution of the computed solution. The formation of plumes is clearly slower than in the previous example (compare with figure 4), which is an expected consequence of halving the amount of cells ($\beta = 10$, $\gamma = 10^3$ instead of $\beta = 20$, $\gamma = 2 \times 10^3$). As one can see, the solution starts developing instabilities at the lower edge of the surface high-concentration layer at around $t = 0.2$. At time $t = 0.3$, three plumes are emerging according to the small modulations in the initial data (5.1).
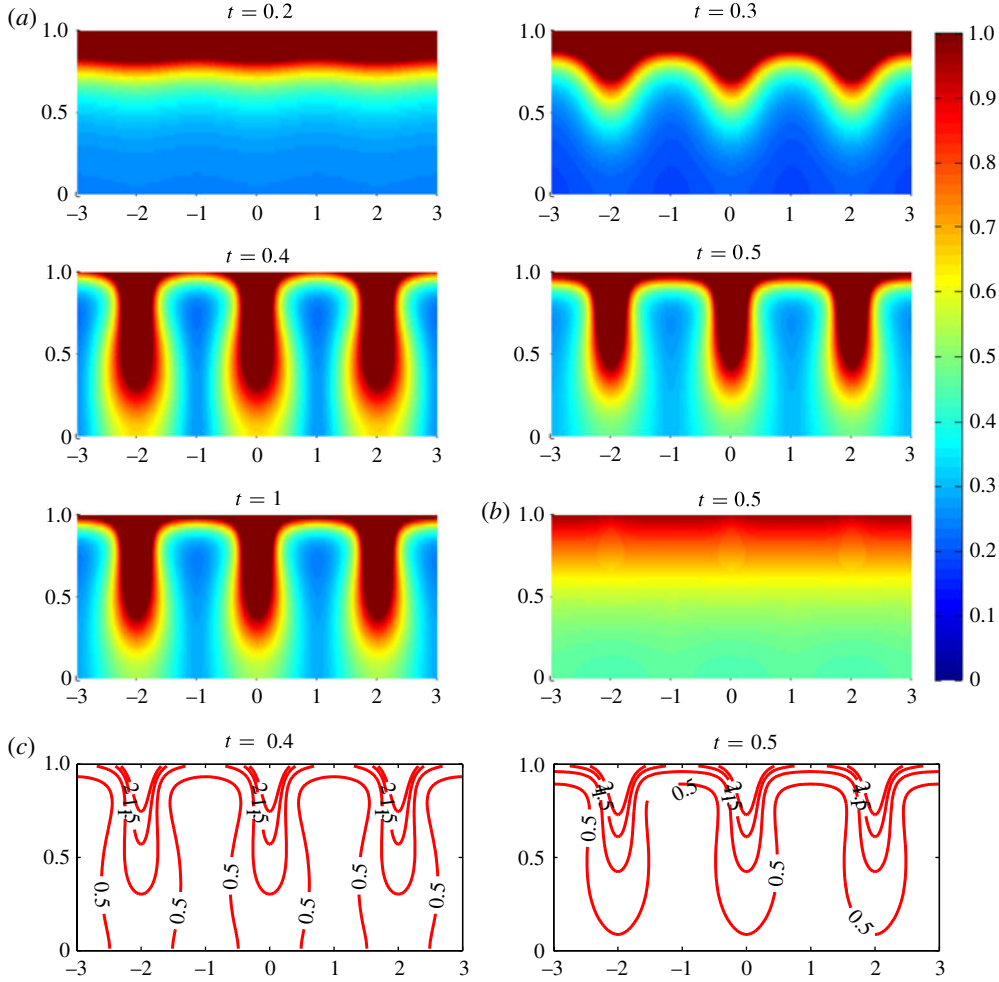
FIGURE 6. Cell density n and oxygen concentration c of the solution of (2.3)–(2.6) with initial data (5.1) and $\beta = 10$, $\gamma = 10^3$ and (3.1). At time $t = 0.2$, the small modulations of the initial data (5.1) turned into visible instabilities at the lower edge of a high-concentration layer near the oxygen-rich surface. At $t = 0.3$, three plumes sink and reach the bottom of the domain at $t = 0.4$ before bouncing back upwards at $t = 0.5$ and reaching a stationary shape by the time $t = 1$. To highlight and colour the plumes in the clearest way, all large values of $n \geqslant 1$ are drawn equally red. The oxygen concentration c at $t = 0.5$ shows that cut-off oxygen level $c = 0.3$ is not approached. (*a*) Formation of stationary plumes. The cell density n at times $t = 0.2, 0.3, 0.4, 0.5, 1$. (*b*) The oxygen density c (plotted at time $t = 0.5$) remains always above the cut-off $c^* = 0.3$. (*c*) Bouncing of the plumes. Level sets of the cell density n at times $t = 0.4, 0.5$.

These plumes reach the bottom of the domain by the time $t = 0.4$, before slightly bouncing upwards again (see the graph at time $t = 0.5$). This temporary bouncing of the plumes can be seen more clearly in the plots of the level sets of the cell density n (figure 6*b*). The plot of the oxygen concentration c at $t = 0.5$, shown in figure 6(*b*), confirms that the oxygen level remains clearly above the cut-off threshold $c^* = 0.3$ on the whole domain (although decaying towards the bottom). The following time evolution (from $t = 0.5$ till $t = 1$) shows only a small change in the shape or size

of the plumes and we conjecture that at $t = 1$ one can already see three numerically stable stationary plumes, which reach the bottom of the domain in the absence of an oxygen cut-off (the simulations have been run till $t = 4$ and showed no change in the obtained solution). We remark that *these plumes form a fully nonlinear stationary state*, which is not covered, for instance, by the weakly nonlinear theory of Metcalfe & Pedley (1998).

Figure 7 illustrates the effects of convection and chemotaxis in shaping and stabilising the stationary plumes. In figure 7(*a*), we plot the time evolution of the kinetic energy $\|\boldsymbol{u}(\cdot, t)\|_{L_x^2(\Omega)}$. With zero initial fluid velocity (see (5.1)) and thus zero initial kinetic energy, a strong increase in kinetic energy is caused once the plumes have started to sink. At the time the plumes have reached the bottom, a maximum of kinetic energy is attained. Later on, the kinetic energy bounces back down and oscillates before levelling at a stationary value.

The velocity field $\boldsymbol{u}$ at time $t = 0.5$ is depicted in figure 7(*b*) for the left of the three plumes whose position is indicated by the level set of the cell density $n = 0.7$. Obviously, the high concentration of cells within the plumes forces the incompressible fluid downwards to the bottom from where it resurfaces in the areas in between the plumes, where there are fewer cells and, thus, a smaller gravitational force is acting on the fluid (see the right-hand side of (2.5)).

While figure 7(*b*) shows clearly how the shape of the plumes and the gravitational forcing of the fluid generate the fluid convection around the plumes, it is not at all obvious how convection, diffusion and chemotaxis shape the stationary plumes themselves. In particular, we remark that while in a vertical slice through a stationary plume the upwards-directed chemotaxis might be able to balance gravity, no such balance can exist in a horizontal direction in which the chemotaxis should, rather, move the cells away from the plumes towards areas where fewer cells have consumed less oxygen. Diffusion too (whose significant effects are clearly visible when comparing the bottom part of figure 4 where the oxygen cut-off stops the chemotaxis with figure 6 where there is no oxygen cut-off) should only act to widen the stationary plumes horizontally. Both these comments are confirmed by figure 7(*c*) which plots the chemotaxis/diffusion component of the cell flux $-\nabla n + \alpha n \nabla c$ together with the level sets $n = 0.3, 0.45, 0.7$ at time $t = 0.5$ and illustrates that the chemotaxis/diffusion flux acts mostly to retract and somewhat to widen the shape of a stationary plume.

Consequently, we conjecture that a stationary plume is predominately shaped by the surrounding fluid convection itself. The fluid component of the cell flux $\boldsymbol{u}n$ together with the level sets $n = 0.3, 0.45, 0.7$ at time $t = 0.5$ are plotted in figure 7(*d*). Moreover, figure 7(*e*) shows the relative strength of the fluid-driven cell flux compared to the chemotaxis/diffusion-component flux, i.e. $|\boldsymbol{u}n|/(|\boldsymbol{u}n| + |-\nabla n + \alpha n \nabla c|)$. It shows that in most areas of the domain (with the exception of the convection vortices) the strength of fluid-driven cell flux dominates the cell flux caused by chemotaxis and diffusion. Finally, figure 7(*f*) depicts several level sets of the strength of the fluid flux $|\boldsymbol{u}n|$. Note that the shape of these level sets agrees well with the shape of the stationary plumes.

Finally, the plots figures 7(*g*) and 7(*h*) show the vector field and the level sets of the total flux $\boldsymbol{u}n - \nabla n + \alpha n \nabla c$. Note that for the stationary plumes the total flux is not zero (in fact it is of the order of the fluid-driven flux figure 7*d*) although it has to be divergence-free.

Altogether, the plots in figure 7 demonstrate that the fluid-driven cell flux is responsible for the shape of the plumes. However, it remains to show how the plumes
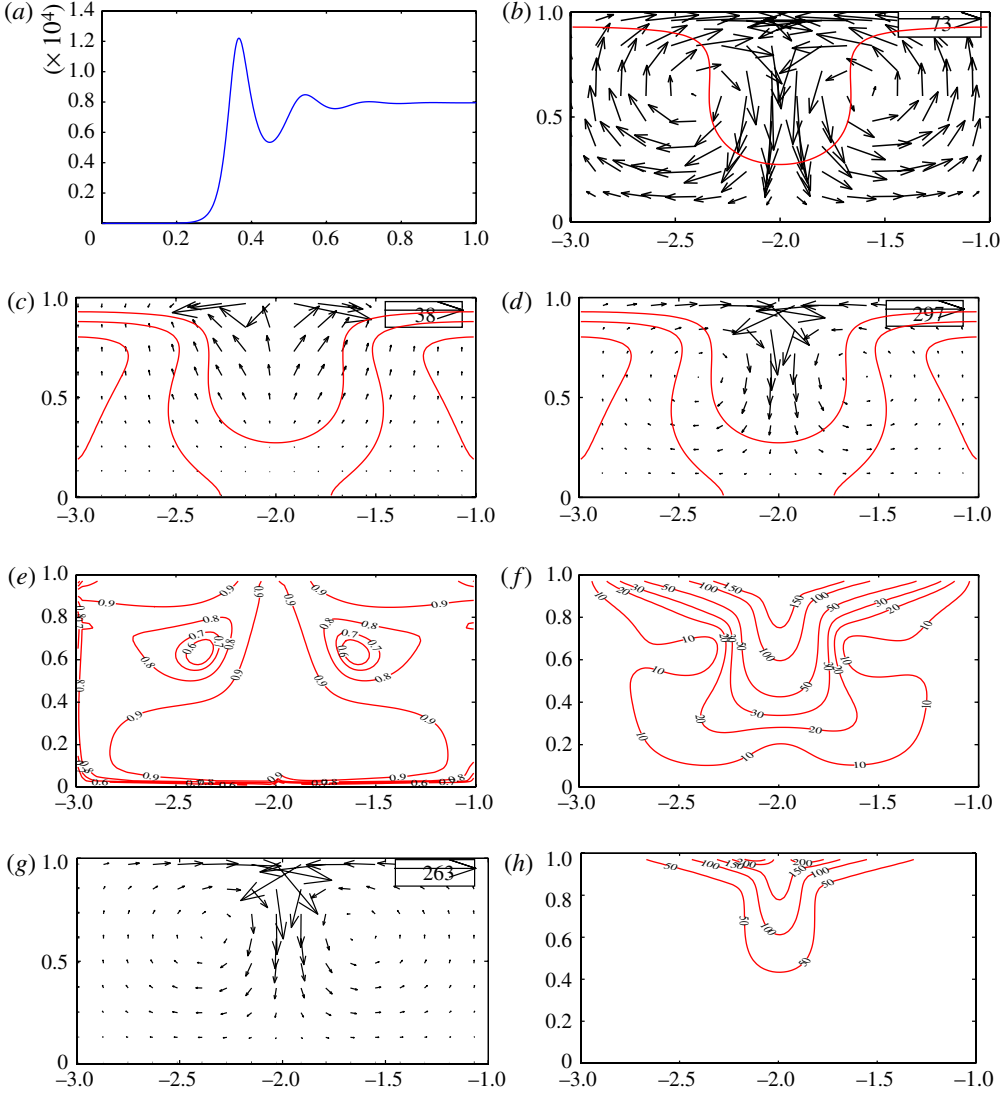
FIGURE 7. (Colour online) The kinetic energy $\|\boldsymbol{u}\|_{L^2_x(\Omega)}$ of the solution of (2.3)–(2.11) with the initial data (5.1) and parameters $\beta = 10$, $\gamma = 10^3$ and (3.1); the velocity field $\boldsymbol{u}$ and various components of the cell-flux around a stationary plume. (a) Time-evolution of kinetic energy $\|\boldsymbol{u}\|_{L^2_x(\Omega)}$. (b) Velocity field $\boldsymbol{u}$ with the level sets $n = 0.7$ at time $t = 0.5$. (c) Chemotaxis/diffusion-component of the cell-flux $-\nabla n + \alpha n \nabla c$ with the level sets $n = 0.3, 0.45, 0.7$ at time $t = 0.5$. (d) Fluid-driven cell-flux $\boldsymbol{u}n$ with the level sets $n = 0.3, 0.45, 0.7$ at time $t = 0.5$. (e) Relative strength of the fluid-driven to the chemotaxis/diffusion flux $|\boldsymbol{u}n|/(|\boldsymbol{u}n| + |-\nabla n + \alpha n \nabla c|)$ at time $t = 0.5$. (f) Level sets of $|\boldsymbol{u}n|$ at time $t = 0.5$. (g) The total flux $\boldsymbol{u}n - \nabla n + \alpha n \nabla c$ at time $t = 0.5$. (h) Level sets of the total flux $\boldsymbol{u}n - \nabla n + \alpha n \nabla c$ at time $t = 0.5$.

can remain stationary since ultimately the only possible energy source to keep the fluid convection flowing is the chemotaxis, which is driven by the oxygen influx at the surface. At the same time, figure 7(c) seems to show that the chemotactic flux $\alpha n \nabla c$ near the surface is even less strong than the diffusion flux $-\nabla n$ since the combined
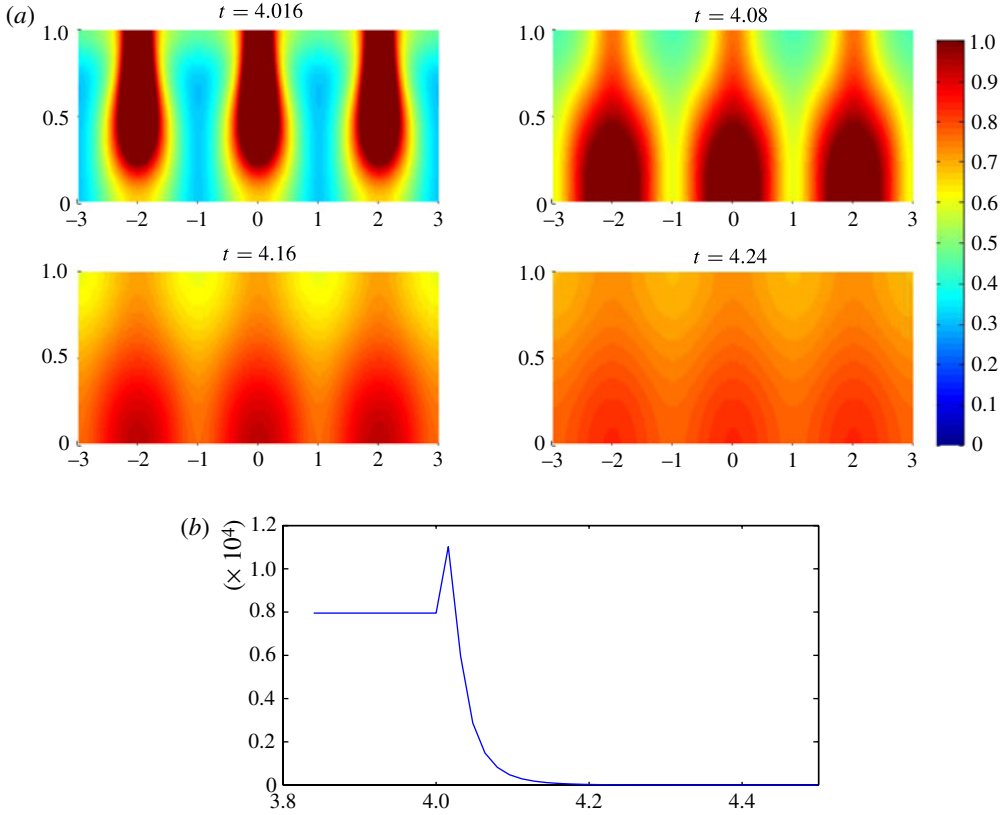
FIGURE 8. Switching off chemotaxis: cell density n of the solution of (2.3)–(2.11) with initial data (5.1) and $\beta = 10$, $\gamma = 10^3$ and (3.1). To highlight and colour the plumes in the best way, all large values of $n \geqslant 1$ are drawn equally red. (*a*) Switching-off chemotaxis: depletion of the high-cell-concentration layer near the surface and diffusion of the plumes. (*b*) Time evolution of fluid kinetic energy $\|\boldsymbol{u}\|_{L^2_{\bar{x}}(\Omega)}$ after switching-off the chemotaxis at time $t = 4$.

chemotaxis/diffusion flux $-\nabla n + \alpha n \nabla c$ points downwards from the surface, which shows that the high-concentration layer is actually compressed by the upstreaming fluid.

In order to show the crucial contribution of the chemotaxis, we completely switched off the chemotaxis at time $t = 4$. A subsequent evolution of the plumes (for $t > 4$) is illustrated in figure 8, which clearly shows that without chemotaxis the high-cell-concentration layer near the surface runs out of cells very quickly as they sink down to the bottom via the plumes. Moreover, the diffusion seems to become the dominating effect, which quickly blurs the shape of the plumes. Figure 8(*b*) shows that the kinetic energy quickly relaxes to zero after chemotaxis is switched off. However, there is an interesting short-time peak in the kinetic energy just after the switching-off, which seems to coincide with the disappearance of the high-cell-concentration layer near the surface in the absence of chemotaxis.

Altogether, we conclude that the numerically stable steady state at time $t = 1$, as plotted in figure 6, results from a subtle balance of chemotaxis, diffusion and the fluid convection, which is driven by gravity (i.e. the sinking of the cells within the plumes) and powered by the chemotaxis and the oxygen influx at the surface, which keeps
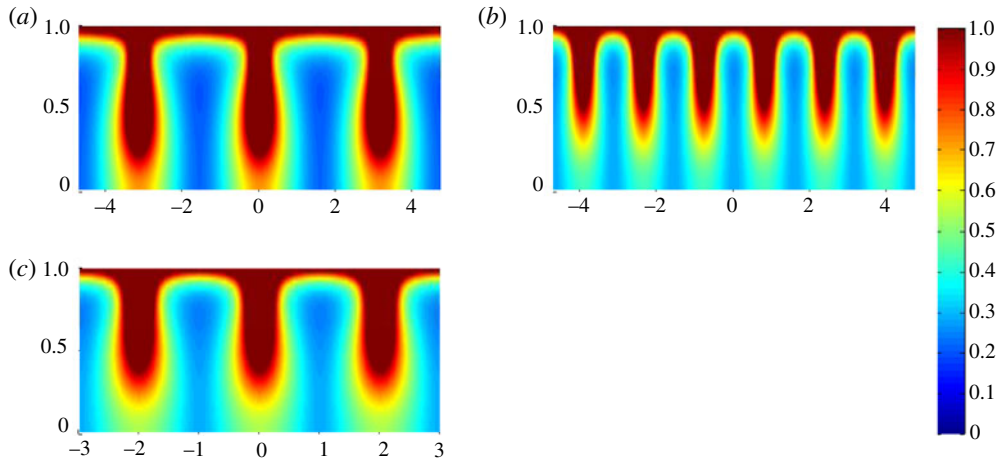
FIGURE 9. Comparison of cell density n of stationary solutions at time $t = 1$ of (2.3)–(2.6) with initial data (5.2) (*a*), (5.3) (*b*) and $\beta = 10$, $\gamma = 10^3$ and (3.1) on the modified domain $[-1.5\pi, 1.5\pi] \times [0, 1]$ in comparison to the standard domain size $[-3, 3] \times [0, 1]$ (*c*).

the oxygen levels above the cut-off and the cells chemotactically active. Moreover, we remark that at present we are not able to prove analytically that the numerical solution at time $t = 4$ is indeed a nonlinearly stable stationary state. However, the observed numerical stability very strongly suggests so.

5.3. *Variation of the domain size and plumes formation*

Figure 9 shows that the qualitative features of the solution are preserved when changing the domain from $[-3, 3] \times [0, 1]$ to $[1.5\pi, 1.5\pi] \times [0, 1]$. Using the initial data

$$n_0(x, y) = \begin{cases} 1 & \text{if } y > 0.499 - 0.01 \sin(2x - 1.5\pi), \\ 0.5 & \text{otherwise,} \end{cases} \quad c_0(x, y) = 1, \boldsymbol{u}_0(x, y) = \boldsymbol{0}.$$

$$(5.2)$$

to trigger three plumes and the initial data

$$n_0(x, y) = \begin{cases} 1 & \text{if } y > 0.499 - 0.01 \sin(4x - 4.5\pi), \\ 0.5 & \text{otherwise,} \end{cases} \quad c_0(x, y) = 1, \boldsymbol{u}_0(x, y) = \boldsymbol{0}.$$

$$(5.3)$$

to trigger six plumes we calculate stationary states with three, respectively six, plumes.

5.4. *Mesh-refinement study*

We conclude this section by a comparison of the numerical results for several refined meshes. In particular, the above plots use a 300×50 grid, and we recalculated them with 240×40, 480×80 and 600×100 grid points. In figure 10, we plot the L^1- and the L^∞-errors of the cell-density n calculated on the 240×40 mesh (figure 10*a*) and on the 480×80 mesh (figure 10*b*) in comparison to the finest 600×100 mesh. We observe a good convergence of the numerical scheme for refined meshes. In particular,
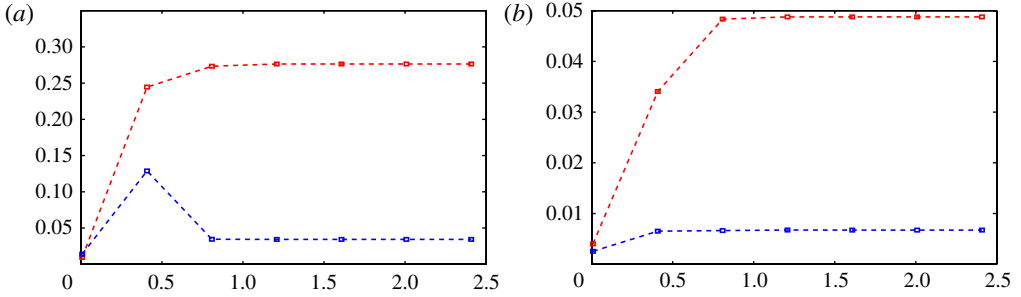
FIGURE 10. Convergence of the numerical solution under mesh refinement: L^1-error (blue line) and L^∞-error (red line) of the cell density n calculated on (*a*) the 240×40 grid compared to the 600×100 grid and (*b*) the 480×80 grid compared to the 600×100 grid.

the formation of stationary plumes, as plotted in figure 6, occurs in a very similar manner on all considered meshes.

6. Stationary plumes in the presence of the oxygen cut-off for high-density data

In this section, we shall study the effects of the oxygen cut-off on the formation and stability of plumes by simply increasing the amount of cells.

6.1. *Parameters and initial data*

We consider the same setting as in §5, but here $\beta = 10^2$ and $\gamma = 10^4$, which corresponds to a 10-times higher reference cell density n_r.

Time evolution: finger-shaped plumes turn into mushroom-shaped plumes

In figure 11, at time $t = 0.03$ we observe a high-concentration layer near the surface (thinner than in figure 6 above) on top of an intermediate depletion area with few cells and a medium-density bottom layer. The cells of the bottom layer are inactive as they have already consumed the oxygen c down to the cut-off level of $c = 0.3$ (as a result of the ten-fold increase in the initial amount of cells compared to figure 6 above). Moreover, we see the onset of plumes appearing (again more narrow than in figure 6).

At time $t = 0.04$, these plumes have sunk halfway down to the bottom and show a finger-like shape. At time $t = 0.05$, as the plumes sink further down into the bottom layer of inactive cells, the oxygen cut-off renders the cells inactive and they behave like a passive suspension of particle. At the same time the finger-like plumes flare out into mushroom-shaped plumes as is known for such suspensions.

Later, at time $t = 0.06$, the lower, mushroom-shaped part of the plumes starts to get blurred by the diffusion and by time $t = 0.1$, diffusion has become the dominating effect for the inactive cells in the bottom half of the domain and the former plumes have been blurred into a homogeneous suspension. In contrast, the three finger-like plumes in the top half of the domain appear to constitute a numerically stable pattern similar to the one obtained in the previous example and shown in figure 6.

We remark that in comparison to experiments like those of figure 1, figure 11 reproduces the high-concentration layer near the surface, the depletion area, the bottom layer of inactive cells as well as the finger-like shape of the plumes within the depletion layer and the mushroom-like shape of the plumes entering the bottom layer.
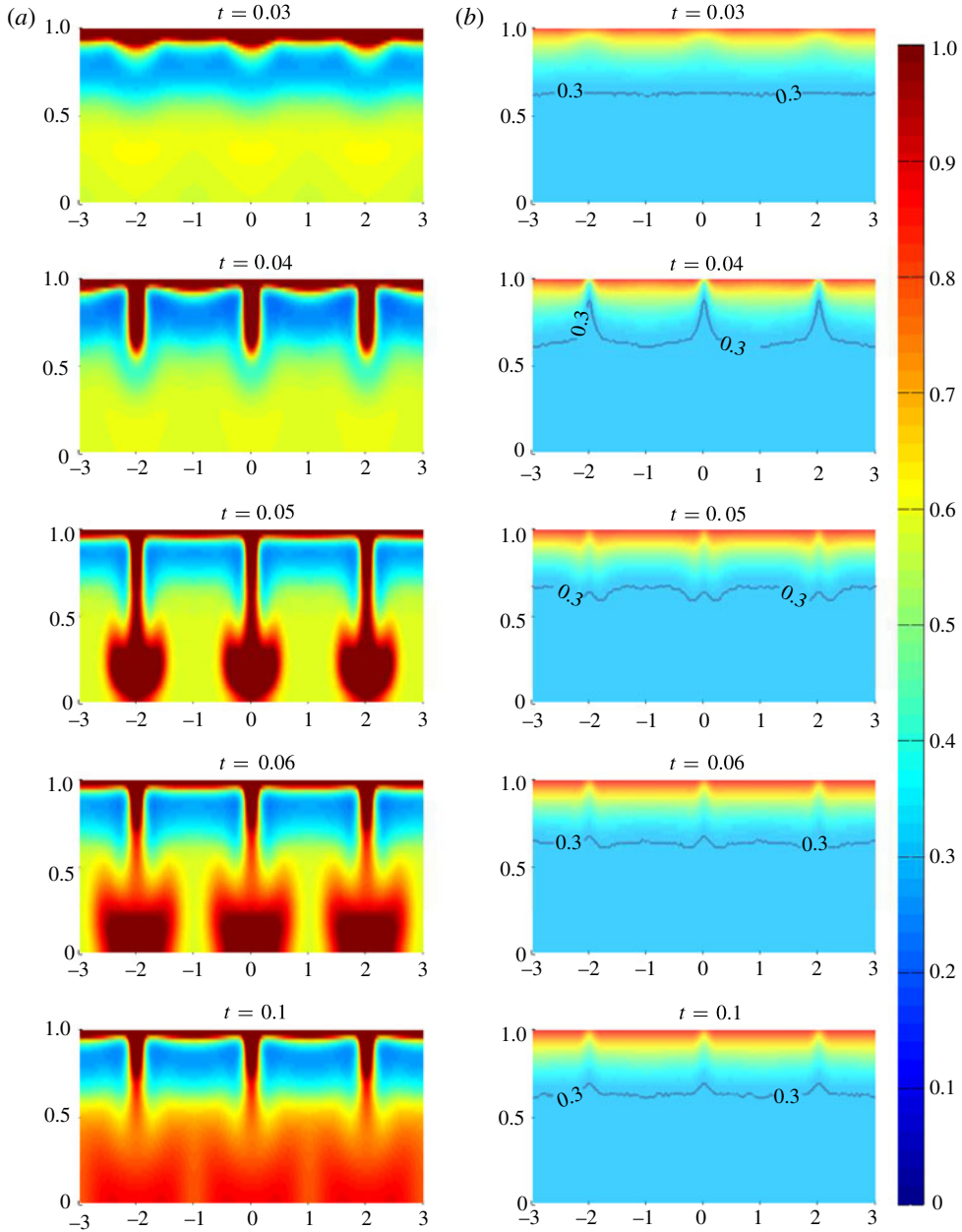
FIGURE 11. Solution (of (2.3)–(2.6), (5.1) with $\beta = 10^2$, $\gamma = 10^4$ for the (*a*) *n*- and (*b*) *c*-components. To best highlight the plumes, all values of $n \geqslant 1$ are drawn equally red.

One difference between figure 11 and figure 1 is that the experiment in figure 1 shows a more irregular spacing of the plumes. However, a more irregular spacing of the plumes could be obtained by including random perturbations into the initial data as was done in §4. A second difference is that the plumes in the experiment figure 1 are somewhat bent in contrast to the straight plumes in the simulation figure 11. This is very likely to be a perturbative effect caused by the non-zero initial velocity field in the experimental set-up.
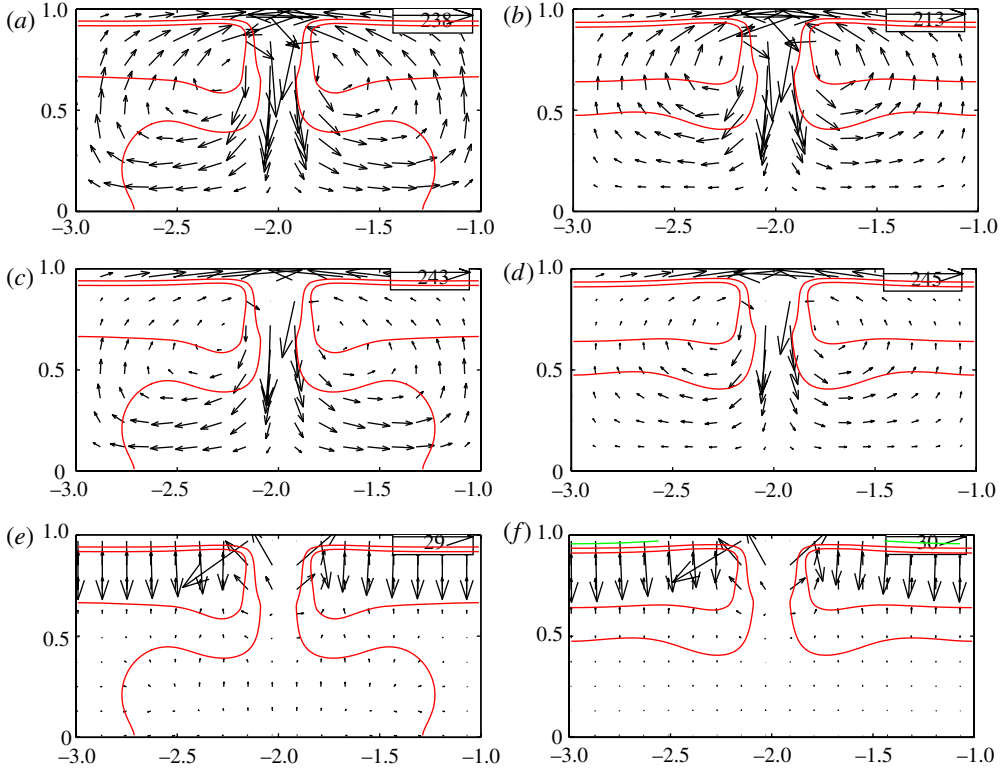
FIGURE 12. (Colour online) Fluid velocity field, fluid-driven cell flux and chemotaxis/diffusion cell flux at times $t = 0.06$ and $t = 0.1$ of the solution of (2.3)–(2.6), (5.1) with $\beta = 10^2$, $\gamma = 10^4$. In order to obtain readable plots of the fluid flux and the chemotaxis/diffusion flux, only the arrows up to a length of 1/3 of the maximal flux strength are plotted. (*a,b*) Fluid velocity $\boldsymbol{u}$ with the level sets $n = 0.45, 0.7$ at time $t = 0.06$ (*a*) and $t = 0.1$ (*b*). (*c,d*) Fluid-driven cell-flux $\boldsymbol{u}n$ with level sets $n = 0.45, 0.7$ at time $t = 0.06$ (*c*) and $t = 0.1$ (*d*). (*e,f*) Chemotaxis/diffusion flux $-\nabla n + \alpha n \nabla c$ with the level sets $n = 0.45, 0.7$ at time $t = 0.06$ (*e*) and $t = 0.1$ (*f*).

Figure 12 illustrates the analysis of the convection pattern observed in figure 11. In particular, we compare (for the left of the three plumes) the fluid velocity $\boldsymbol{u}$, the fluid-driven cell flux $\boldsymbol{u}n$ and the chemotaxis/diffusion flux $-\nabla n + \alpha n \nabla c$ at the times $t = 0.06$ (left column of figure 12) and $t = 0.1$ (right column of figure 12). We note that in order to obtain better scaling of the plots of the fluid flux and the chemotaxis/diffusion flux, only the arrows up to a length of 1/3 of the maximal flux strength were plotted while the remaining arrows were omitted. Moreover, we have included the cell-density level sets $n = 0.45, 0.7$ in the plots. At time $t = 0.06$, we observe that the sinking of the plumes stirs the fluid down to the bottom of the domain as previously depicted in figure 11. Later at time $t = 0.1$, however, the fluid convection has shifted (in contrast to figure 11) upwards from the bottom and away from the bulk of inactive cells there. Presumably, there is not enough energy provided by the chemotaxis in order to stir up cells from all of the domain. As a consequence, only close to the surface, where the oxygen concentration remains above the threshold, does the fluid convection keep confining the plumes against the chemotaxis and diffusion and renders them stationary. This shows again that it is ultimately the chemotaxis (i.e. the cells swimming upwards
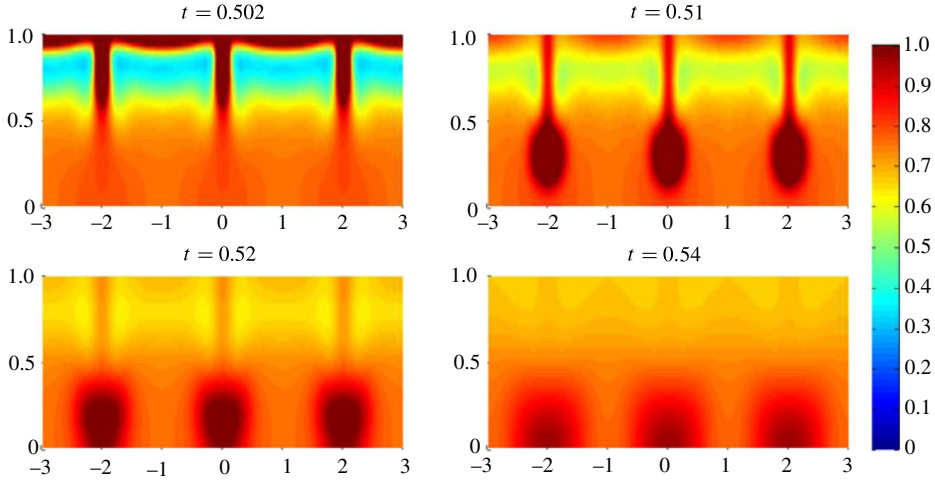
FIGURE 13. Switching off the chemotaxis: cell density n and oxygen concentration c of the solution of (2.3)–(2.11), (5.1) with $\beta = 10^2$, $\gamma = 10^4$. To best highlight the plumes, all values of $n \geqslant 1$ are drawn equally red.

in between the plumes and refeeding the high-concentration layer near the surface) and not the gravity (making the cells sink down within the plumes), which is the driving force of the fluid convection and thus responsible for the existence of numerically stable stationary plumes. Once again, note how the fluid flux $\boldsymbol{u}n$ compresses the high-concentration surface layer as the chemotaxis/diffusion flux near the surface layer is dominated by $-\nabla n$, which points downwards from the surface.

Finally, figure 13 shows the effects of switching off the chemotaxis (at time $t = 0.5$). As in the previous example, we observe that without the chemotaxis refeeding cells into the surface layer, the fluid convection collapses quickly, the finger-shaped plumes sink into the bottom half and get blurred by the diffusion.

6.2. *Comparison of different oxygen thresholds $c^* = 0.2, 0.3, 0.4$.*

Figure 14 illustrates the influences of the oxygen threshold c^* on the calculated cell density. It shows that the qualitative features of the solution are very well preserved when changing the threshold value for the oxygen cut-off c^*.

7. How finger-shaped plumes turn into mushroom-shaped plumes

In comparison with the previous example, in this section, we demonstrate the sinking of plumes undisturbed by effects of the surrounding cells.

Parameters and initial data

We thus consider the same parameters as in the previous section, but choose initial data without cells in the lower region of the domain:

$$n_0(x, y) = \begin{cases} 1 & \text{if } y > 0.499 - 0.01 \sin((x - 1.5)\pi), \\ 0 & \text{otherwise}, \end{cases} \qquad c_0(x, y) = 1, \, \boldsymbol{u}_0(x, y) = \boldsymbol{0}, \quad (7.1)$$
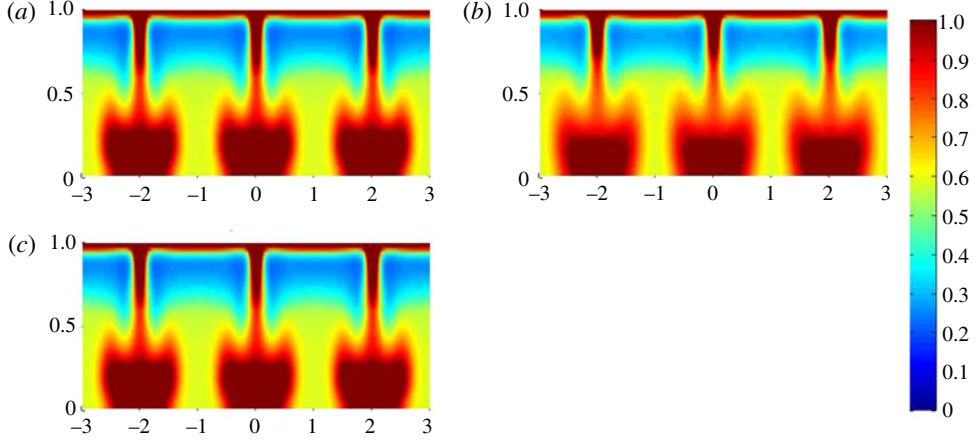
FIGURE 14. Comparison of the cell density n of (2.3)–(2.6), (5.1) with $c^* = 0.2$ (*a*), with $c^* = 0.3$ (*b*) and $c^* = 0.4$ (*c*), for $\beta = 10^2$, $\gamma = 10^4$ and $t = 0.06$. To best highlight the plumes, all values of $n \geqslant 1$ are drawn equally red.
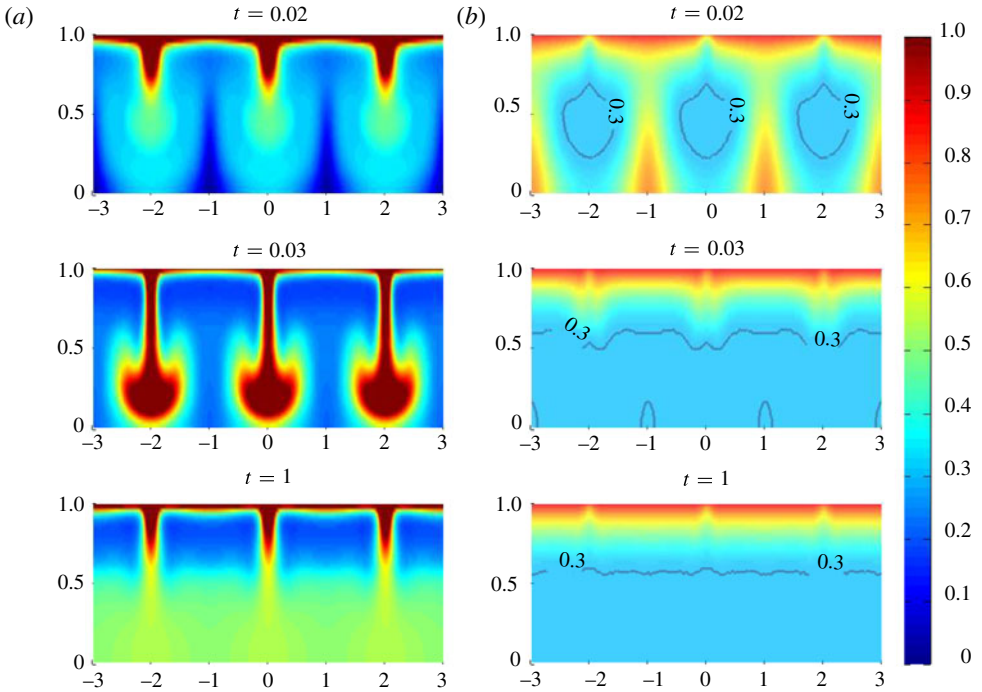

FIGURE 15. Solution of (2.3)–(2.6), (7.1) with $\beta = 10^2$, $\gamma = 10^4$ for (*a*) the n- and (*b*) the c-components.

7.1. *Time evolution: from fingers to mushrooms to fingers*

The time snapshots of computed solution (the n- and c-components) are plotted in figure 15. A very similar computation with the diffusion coefficient for n diminishing from D_n to $D_n/10$ for c below c^* is shown in appendix B. One can clearly see the appearance of a high-concentration layer near the surface and an early stage of falling
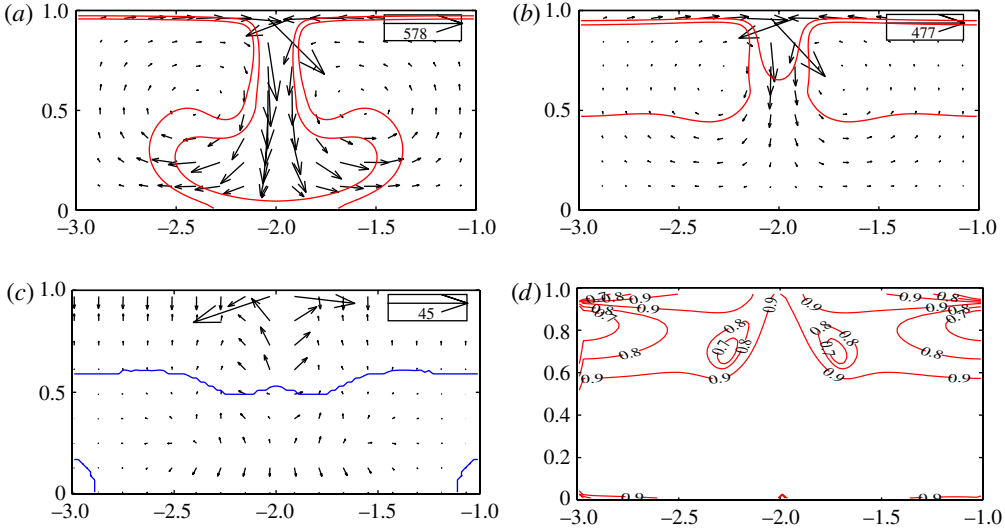
FIGURE 16. (Colour online) Fluid-driven cell-flux at times $t = 0.03$ and $t = 1$ as well as the chemotaxis/diffusion cell-flux at time $t = 0.03$ and the relative strength of fluid to chemotaxis/diffusion flux at $t = 0.1$ of the solution of (2.3)–(2.6), (7.1) with $\beta = 10^2$, $\gamma = 10^4$. (*a*) Fluid-driven cell flux $\boldsymbol{u}n$ with level sets $n = 0.45, 0.7$ at time $t = 0.03$. (*b*) Fluid-driven cell flux $\boldsymbol{u}n$ with level sets $n = 0.45, 0.7$ at time $t = 1$. (*c*) Chemotaxis/diffusion flux $-\nabla n + \alpha n \nabla c$ with cut-off level set $c = 0.3$ (inner area) at time $t = 0.03$. (*d*) Contours of relative strength of fluid-chemotaxis flux $|\boldsymbol{u}n|/(|\boldsymbol{u}n| + |-\nabla n + \alpha n \nabla c|)$ at time $t = 1$.

plumes at time $t = 0.02$. Nevertheless, by this time the plumes have already consumed in their proximity the oxygen down to the cut-off concentration $c^* = 0.3$. By time $t = 0.03$, all of the oxygen in the lower part of the domain has been consumed down to the cut-off and the plumes flare out into a mushroom-type shape, whose onset might have already been present at time $t = 0.02$. Finally, at time $t = 1$, the lower part of the domain has diffused into a rather homogeneous suspension of inactive cells. This is in contrast to the upper half of the domain, where the chemotaxis of the active cells maintains the fluid convection, which in turn confines the plume to their shape.

In figures 16(*a*) and 16(*b*), we plot the fluid-driven cell flux $\boldsymbol{u}n$ for the left of the three plumes at times $t = 0.03$ and $t = 1$. At $t = 0.03$, when the sinking plumes have reached the bottom, there is a significant cell flux in the lower half of the domain, which however is strongly diminished by $t = 1$.

Figure 16(*c*) shows the chemotaxis/diffusion flux together with the oxygen level set $c = 0.3$ (lines) plotted at time $t = 0.03$. Inside the lines, where chemotaxis is turned off, it is the diffusion flux that blurs the plume. One can see that there is only a relatively small area outside the blue lines, where the chemotaxis/diffusion flux is directed upwards and helps feed cells into the concentration layer near the surface and, thus, into the sinking plume. We conjecture that this small area is responsible for the lack of strength of the resulting fluid convection to keep stirring the cells in the bottom layer for large times. We remark that like in the previous example, the chemotaxis/diffusion flux near the surface and away from the plume is dominated by the fluid flux, which points downwards as the fluid compresses the high-concentration layer.

Figure 16(*d*) shows the relative strength of the fluid cell flux to the chemotaxis/diffusion cell flux. It should be observed that it is unclear whether the

solution at time $t = 1$ (see figure 15) can constitute a stationary state. Indeed, one can see that some cells sink from the high-concentration plumes at the upper half down to the bottom of the domain, which could result in all the cells eventually sinking down. We conjecture, however, that this loss of cells down to the bottom is compensated by the fluid convection stirring inactive cells in between the plumes up into areas outside the oxygen cut-off.

7.2. *Overall oxygen consumption due to bio-convection*

It is interesting consider about the overall oxygen consumption of the cells due to the bio-convection pattern: first note that the cell-density equation (2.3) with the boundary conditions (2.11) conserves the initial total number of particle/cells, i.e. $\int_{\Omega} n(t, x, y) \, dx \, dy = \int_{\Omega} n_0(x, y) \, dx \, dy$ for all $t \geqslant 0$. Moreover, integrating the oxygen-concentration equation (2.4) with the boundary conditions (2.11) yields for any stationary solution that the total oxygen influx through the surface equals β times the total mass of chemotactically active cells, i.e.

$$\int_{Surface} \delta c_y^s(x, 1) \, dx = \beta \int_{\Omega} r(c^s) \, n^s(x, y) \, dx \, dy, \tag{7.2}$$

where $c^s(x, y)$ and $n^s(x, y)$ denote the oxygen and cell concentration of the stationary solution.

Recalling that the length of the surface $|Surface|$ equals the area of the domain $|\Omega|$, we obtain equally that the averaged oxygen influx per surface unit divided by the averaged cell mass per unit area equals the relative mass of the active cells compared to the total mass of cells, i.e.

$$\frac{\int_{Surface} \delta c_y^s(x, 1) \, dx}{\int_{\Omega} n^s(x, y) \, dx \, dy} = \beta \frac{\int_{\Omega} r(c^s(x, y)) \, n^s(x, y) \, dx \, dy}{\int_{\Omega} n^s(x, y) \, dx \, dy}. \tag{7.3}$$

Thus, for stationary patterns without oxygen cut-off (these are the homogeneous-in-y pattern in figure 2 and the cases with three and six stationary plumes, see figure 9) the overall oxygen consumption, which is expressed in terms of the total oxygen influx through the surface, equals β times the total initial cell mass.

For the stationary convection pattern with oxygen cut-off we calculate the following numbers: in figure 14 comparing stationary pattern with $c^* = 0.2, 0.3, 0.4$ we find that, respectively, 39.4 %, 37.5 %, and 35.1 % of the cells are active:

$$\frac{\int_{Surface} \delta c_y^s(x, 1) \, dx}{\int_{\Omega} n^s(x, y) \, dx \, dy} = \beta \, (0.394, 0.375, 0.351) \quad \text{for } c^* = (0.2, 0.3, 0.4). \tag{7.4}$$

In contrast we find for figure 15 that 44.3 % of the cells are active. Note that 44.3 % is a significant increase in active cells of the stationary pattern compared to figure 14 were we found for $c^* = 0.3$ a stationary pattern with only 37.5 %. In fact, this difference is stronger than the variation of the threshold $c^* = 0.2, 0.3, 0.4$ in figure 14 and is entirely due to the modified initial data (7.1), which feature no cells in the bottom of the domain in contrast to the initial data (5.1), which were used for figure 14.

Acknowledgements

Appendix A. Derivation of the numerical method

We start by writing the system (2.3)–(2.6) in coordinate form and rewrite the ω-equation in an equivalent non-conservative (transport) form:

$$n_t + [(u + \alpha r(c)c_x)n]_x + [(v + \alpha r(c)c_y)n]_y = n_{xx} + n_{yy}, \tag{A 1}$$

$$c_t + (uc)_x + (vc)_y = \delta(c_{xx} + c_{yy}) - \beta r(c)n, \tag{A 2}$$

$$\omega_t + u\omega_x + v\omega_y = Sc(\omega_{xx} + \omega_{yy}) - \gamma\, Sc\, n_x, \tag{A 3}$$

$$\psi_{xx} + \psi_{yy} = -\omega. \tag{A 4}$$

In this system the oxygen concentration c and the vorticity ω are convected by the flow, diffused and affected by the source terms (the oxygen uptake term $-\beta r(c)n$ and the gravity term $-\gamma\, Sc\, n_x$, respectively). The evolution of the cell concentration n is governed by convection–chemotaxis fluxes, $(u + \alpha r(c)c_x)n$ and $(v + \alpha r(c)c_y)n$, and the linear diffusion term.

In the numerical method presented, the quantities n and c will be evolved in time by solving the chemotaxis equations (A 1) and (A 2) using the second-order finite-volume upwind method, while ω will be evolved on a staggered grid by applying the second-order centred-difference scheme to the vorticity equation (A 3). Therefore, the resulting method will be a hybrid finite-volume finite-difference scheme. The velocities u and v will be recovered from the stream-function ψ by solving the elliptic equation (A 4) followed by the centred-difference approximations of the velocities in $u = \psi_y$ and $v = -\psi_x$.

A.1. *Finite-volume upwind scheme for the chemotaxis equations*

We first describe a semi-discrete second-order finite-volume upwind scheme for (A 1), (A 2). We divide the computational domain Ω into the cells $C_{j,k} := [x_{j-(1/2)}, x_{j+(1/2)}] \times [y_{k-(1/2)}, y_{k+(1/2)}]$ of size $\Delta x \Delta y$ (see figure 17), where Δx and Δy are small spatial scales assumed, for simplicity, to be constants. We then denote the cell averages of $\boldsymbol{q} := (n, c)^{\mathrm{T}}$ by

$$\overline{\boldsymbol{q}}_{j,k}(t) = \frac{1}{\Delta x \Delta y} \iint_{C_{j,k}} \boldsymbol{q}(x, y, t)\, \mathrm{d}x\, \mathrm{d}y, \tag{A 5}$$
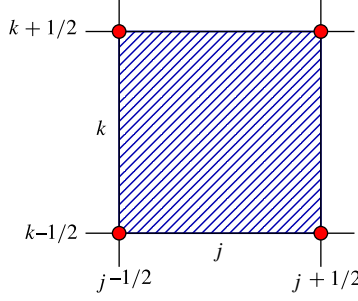
FIGURE 17. (Colour online) Typical finite-volume cell $C_{j,k}$ for the evolution of cell averages $\bar{n}$ and $\bar{c}$. Point values of ω and ψ are computed at the 'corners' of the cell.

and integrate (A 1), (A 2) over cell $C_{j,k}$ to obtain

$$
\Delta x \Delta y \frac{\mathrm{d}}{\mathrm{d}t} \bar{n}_{j,k} + \int_{y_{k-(1/2)}}^{y_{k+(1/2)}} (u + \alpha r(c)c_x)n \bigg|_{x_{j-(1/2)}}^{x_{j+(1/2)}} \mathrm{d}y + \int_{x_{j-(1/2)}}^{x_{j+(1/2)}} (v + \alpha r(c)c_y)n \bigg|_{y_{k-(1/2)}}^{y_{k+(1/2)}} \mathrm{d}x
$$

$$
= \int_{y_{k-(1/2)}}^{y_{k+(1/2)}} n_x \bigg|_{x_{j-(1/2)}}^{x_{j+(1/2)}} \mathrm{d}y + \int_{x_{j-(1/2)}}^{x_{j+(1/2)}} n_y \bigg|_{y_{k-(1/2)}}^{y_{k+(1/2)}} \mathrm{d}x, \tag{A 6}
$$

$$
\Delta x \Delta y \frac{\mathrm{d}}{\mathrm{d}t} \bar{c}_{j,k} + \int_{y_{k-(1/2)}}^{y_{k+(1/2)}} u c \bigg|_{x_{j-(1/2)}}^{x_{j+(1/2)}} \mathrm{d}y + \int_{x_{j-(1/2)}}^{x_{j+(1/2)}} v c \bigg|_{y_{k-(1/2)}}^{y_{k+(1/2)}} \mathrm{d}x
$$

$$
= \delta \int_{y_{k-(1/2)}}^{y_{k+(1/2)}} c_x \bigg|_{x_{j-(1/2)}}^{x_{j+(1/2)}} \mathrm{d}y + \delta \int_{x_{j-(1/2)}}^{x_{j+(1/2)}} c_y \bigg|_{y_{k-(1/2)}}^{y_{k+(1/2)}} \mathrm{d}x - \beta \iint_{C_{j,k}} r(c)n \, \mathrm{d}x \, \mathrm{d}y. \tag{A 7}
$$

Applying the midpoint rule to the above integrals and dividing by $\Delta x \Delta y$ results in

$$
\frac{\mathrm{d}}{\mathrm{d}t} \bar{n}_{j,k} \approx - \frac{(u + \alpha r(c)c_x)n|_{(x_{j+(1/2)},y_k)} - (u + \alpha r(c)c_x)n|_{(x_{j-(1/2)},y_k)}}{\Delta x}
$$

$$
- \frac{(v + \alpha r(c)c_y)n|_{(x_j,y_{k+(1/2)})} - (v + \alpha r(c)c_y)n|_{(x_j,y_{k-(1/2)})}}{\Delta y}
$$

$$
+ \frac{n_x|_{(x_{j+(1/2)},y_k)} - n_x|_{(x_{j-(1/2)},y_k)}}{\Delta x} + \frac{n_y|_{(x_j,y_{k+(1/2)})} - n_y|_{(x_j,y_{k-(1/2)})}}{\Delta y}, \tag{A 8}
$$

$$
\frac{\mathrm{d}}{\mathrm{d}t} \bar{c}_{j,k} \approx - \frac{u c|_{(x_{j+(1/2)},y_k)} - u c|_{(x_{j-(1/2)},y_k)}}{\Delta x} - \frac{v c|_{(x_j,y_{k+(1/2)})} - v c|_{(x_j,y_{k-(1/2)})}}{\Delta y}
$$

$$
+ \delta \frac{c_x|_{(x_{j+(1/2)},y_k)} - c_x|_{(x_{j-(1/2)},y_k)}}{\Delta x} + \delta \frac{c_y|_{(x_j,y_{k+(1/2)})} - c_y|_{(x_j,y_{k-(1/2)})}}{\Delta y}
$$

$$
+ \beta r(\bar{c}_{j,k})\bar{n}_{j,k}. \tag{A 9}
$$

The construction of the scheme will be complete once the fluxes at the cell interfaces in (A 8) and (A 9) are approximated numerically. The semi-discrete finite-volume upwind scheme for computing cell averages $\bar{q}_{j,k} := (\bar{n}_{j,k}, \bar{c}_{j,k})^{\mathrm{T}}$ then can be

written as the following system of ODEs:

$$\frac{\mathrm{d}}{\mathrm{d}t}\overline{\boldsymbol{q}}_{j,k} = -\frac{\boldsymbol{H}^x_{j+(1/2),k} - \boldsymbol{H}^x_{j-(1/2),k}}{\Delta x} - \frac{\boldsymbol{H}^y_{j,k+(1/2)} - \boldsymbol{H}^y_{j,k-(1/2)}}{\Delta y}$$

$$+ \frac{\boldsymbol{P}^x_{j+(1/2),k} - \boldsymbol{P}^x_{j-(1/2),k}}{\Delta x} + \frac{\boldsymbol{P}^y_{j,k+(1/2)} - \boldsymbol{P}^y_{j,k-(1/2)}}{\Delta y} + \overline{\boldsymbol{R}}_{j,k}, \qquad (A\,10)$$

where

$$\boldsymbol{H}^x_{j\pm(1/2),k} \approx ((u + \alpha r(c)c_x)n|_{(x_{j\pm(1/2)},y_k)}, \, u\,c|_{(x_{j\pm(1/2)},y_k)})^{\mathrm{T}} \qquad (A\,11)$$

and

$$\boldsymbol{H}^y_{j,k\pm(1/2)} \approx ((v + \alpha r(c)c_y)n|_{(x_j,y_{k\pm(1/2)})}, \, v\,c|_{(x_j,y_{k\pm(1/2)})})^{\mathrm{T}} \qquad (A\,12)$$

are numerical convection–chemotaxis fluxes,

$$\boldsymbol{P}^x_{j\pm(1/2),k} \approx (n_x|_{(x_{j\pm(1/2)},y_k)}, \, \delta c_x|_{(x_{j\pm(1/2)},y_k)})^{\mathrm{T}} \qquad (A\,13)$$

and

$$\boldsymbol{P}^y_{j,k\pm(1/2)} \approx (n_y|_{(x_j,y_{k\pm(1/2)})}, \, c_y|_{(x_j,y_{k\pm(1/2)})})^{\mathrm{T}} \qquad (A\,14)$$

are centred numerical diffusion fluxes, and $\overline{\boldsymbol{R}}_{j,k} = (0, \beta r(\overline{c}_{j,k})\overline{n}_{j,k})^{\mathrm{T}}$ are the cell averages of the source term. From now on all indexed quantities used in the description of the scheme are calculated at time t, but we suppress their time-dependence in order to shorten the formulae.

To ensure stability of the scheme (A 10), we use an upwind approximation of the convection–chemotaxis fluxes, which can be written in the component-wise form as follows:

$$\boldsymbol{H}^{x,(i)}_{j+(1/2),k} = \begin{cases} a^{(i)}_{j+(1/2),k}\,\boldsymbol{q}^{E,(i)}_{j,k} & \text{if } a^{(i)}_{j+(1/2),k} > 0, \\ a^{(i)}_{j+(1/2),k}\,\boldsymbol{q}^{W,(i)}_{j+1,k} & \text{if } a^{(i)}_{j+(1/2),k} < 0, \end{cases} \quad i = 1, 2, \qquad (A\,15a)$$

$$\boldsymbol{H}^{y,(i)}_{j,k+(1/2)} = \begin{cases} b^{(i)}_{j,k+(1/2)}\,\boldsymbol{q}^{N,(i)}_{j,k} & \text{if } b^{(i)}_{j,k+(1/2)} > 0, \\ b^{(i)}_{j,k+(1/2)}\,\boldsymbol{q}^{S,(i)}_{j,k+1} & \text{if } b^{(i)}_{j,k+(1/2)} < 0, \end{cases} \quad i = 1, 2. \qquad (A\,15b)$$

Here, the upper index $(\cdot)^{(i)}$ stands for the number of the vector component and $\boldsymbol{q}^{E,W,N,S}_{j,k}$ are the point values of the piecewise linear reconstruction,

$$\widetilde{\boldsymbol{q}}(x, y) = \overline{\boldsymbol{q}}_{j,k} + (\boldsymbol{q}_x)_{j,k}(x - x_j) + (\boldsymbol{q}_y)_{j,k}(y - y_k), \quad (x, y) \in C_{j,k}, \qquad (A\,16)$$

at the points $(x_{j+(1/2)}, y_k)$, $(x_{j-(1/2)}, y_k)$, $(x_j, y_{k+(1/2)})$ and $(x_j, y_{k-(1/2)})$, respectively. Namely, we have

$$\boldsymbol{q}^E_{j,k} = \widetilde{\boldsymbol{q}}(x_{j+(1/2)}-, y_k) = \overline{\boldsymbol{q}}_{j,k} + \frac{\Delta x}{2}\,(\boldsymbol{q}_x)_{j,k}, \quad \boldsymbol{q}^W_{j,k} = \widetilde{\boldsymbol{q}}(x_{j-(1/2)}+, y_k) = \overline{\boldsymbol{q}}_{j,k} - \frac{\Delta x}{2}\,(\boldsymbol{q}_x)_{j,k},$$
$$(A\,17a)$$

$$\boldsymbol{q}^N_{j,k} = \widetilde{\boldsymbol{q}}(x_j, y_{k+(1/2)}-) = \overline{\boldsymbol{q}}_{j,k} + \frac{\Delta y}{2}\,(\boldsymbol{q}_y)_{j,k}, \quad \boldsymbol{q}^S_{j,k} = \widetilde{\boldsymbol{q}}(x_j, y_{k-(1/2)}+) = \overline{\boldsymbol{q}}_{j,k} - \frac{\Delta y}{2}\,(\boldsymbol{q}_y)_{j,k}.$$
$$(A\,17b)$$

To ensure the second order of accuracy, the numerical derivatives $(\boldsymbol{q}_x)_{j,k}$ and $(\boldsymbol{q}_y)_{j,k}$ are to be (at least) first-order approximations of the corresponding exact

derivatives $q_x(x_j, y_k, t)$ and $q_y(x_j, y_k, t)$. In our numerical experiments, we have used the central-difference approximations,

$$(q_x)_{j,k} = \frac{\overline{q}_{j+1,k} - \overline{q}_{j-1,k}}{2\Delta x}, \quad (q_y)_{j,k} = \frac{\overline{q}_{j,k+1} - \overline{q}_{j,k-1}}{2\Delta y}, \tag{A 18}$$

throughout the computational domain Ω except for the cells, where the linear approach (A 18) leads to the appearance of negative reconstructed values of n. In the cells, where either $n_{j,k}^E$ or $n_{j,k}^W$ is negative, we replace (A 18) with a nonlinear total variation diminishing (TVD) minmod2 reconstruction (see e.g. Sweby 1984; Nessyahu & Tadmor 1990; Lie & Noelle 2003), which corresponds to

$$(n_x)_{j,k} = minmod\left(2\frac{\overline{n}_{j,k} - \overline{n}_{j-1,k}}{\Delta x}, \frac{\overline{n}_{j+1,k} - \overline{n}_{j-1,k}}{2\Delta x}, 2\frac{\overline{n}_{j+1,k} - \overline{n}_{j,k}}{\Delta x}\right) \tag{A 19}$$

and guarantees that no negative values of n emerge at the reconstruction step. Similarly, if either $n_{j,k}^N$ or $n_{j,k}^S$ is negative, we set

$$(n_y)_{j,k} = minmod\left(2\frac{\overline{n}_{j,k} - \overline{n}_{j,k-1}}{\Delta y}, \frac{\overline{n}_{j,k+1} - \overline{n}_{j,k-1}}{2\Delta y}, 2\frac{\overline{n}_{j,k+1} - \overline{n}_{j,k}}{\Delta y}\right) \tag{A 20}$$

and recalculate the reconstructed values $n_{j,k}^N$ and $n_{j,k}^S$. The minmod function used in (A 19) and (A 20) is defined as

$$minmod(z_1, z_2, \ldots) := \begin{cases} \min_j\{z_j\} & \text{if } z_j > 0 \ \forall j, \\ \max_j\{z_j\} & \text{if } z_j < 0 \ \forall j, \\ 0 & \text{otherwise.} \end{cases} \tag{A 21}$$

To complete the description of the numerical convection–chemotaxis fluxes in (A 15b), we need to specify the quantities $a_{j+(1/2),k}^{(i)}$ and $b_{j,k+(1/2)}^{(i)}$, which are the local speeds in the x- and y-directions, respectively. Since all components of the solution are expected to be smooth, the local speeds can be approximated using the centred differences and averages as

$$a_{j+(1/2),k}^{(1)} = u_{j+(1/2),k} + \alpha r(c_{j+(1/2),k})\,(c_x)_{j+(1/2),k}, \quad a_{j+(1/2),k}^{(2)} = u_{j+(1/2),k}, \tag{A 22}$$

$$b_{j,k+(1/2)}^{(1)} = v_{j,k+(1/2)} + \alpha r(c_{j,k+(1/2)})\,(c_y)_{j,k+(1/2)}, \quad b_{j,k+(1/2)}^{(2)} = v_{j,k+(1/2)}, \tag{A 23}$$

where

$$(c_x)_{j+(1/2),k} := \frac{\overline{c}_{j+1,k} - \overline{c}_{j,k}}{\Delta x}, \quad (c_y)_{j,k+(1/2)} := \frac{\overline{c}_{j,k+1} - \overline{c}_{j,k}}{\Delta y}, \tag{A 24}$$

$$c_{j+(1/2),k} = \tfrac{1}{2}(c_{j,k}^E + c_{j+1,k}^W), \quad c_{j,k+(1/2)} = \tfrac{1}{2}(c_{j,k}^N + c_{j,k+1}^S), \tag{A 25}$$

and $u_{j+(1/2),k}$ and $v_{j,k+(1/2)}$ are given by (A 37).

Finally, the centred numerical diffusion fluxes are

$$P_{j+(1/2),k}^x = \left(\frac{\overline{n}_{j+1,k} - \overline{n}_{j,k}}{\Delta x}, \delta\frac{\overline{c}_{j+1,k} - \overline{c}_{j,k}}{\Delta x}\right)^T \tag{A 26}$$

and

$$P_{j,k+(1/2)}^y = \left(\frac{\overline{n}_{j,k+1} - \overline{n}_{j,k}}{\Delta y}, \delta\frac{\overline{c}_{j,k+1} - \overline{c}_{j,k}}{\Delta y}\right)^T. \tag{A 27}$$

Remark. Previous numerical schemes for aggregating chemotaxis models like the Patlak–Keller–Segel system (see Filbet 2006; Haškovec & Schmeiser 2009; Carrillo & Moll 2009) share in common that they are designed to capture chemotactic blow-up phenomena, which are not relevant for the above system (A 4) where the chemoattractant is consumed not produced by the cell.

Remark. The presented upwind scheme preserves positivity of the cell density n provided the ODE system (A 10) is discretised using a strong stability-preserving (SSP) ODE solver (Gottlieb, Shu & Tadmor 2001; Pareschi & Russo 2005; Higueras & Roldán 2006). This a very important property that any robust numerical method should satisfy. To prove this, it is enough to consider the forward Euler time discretisation of the ODE system (A 10). The fully discrete update for the n-component thus becomes:

$$\bar{n}_{j,k}(t + \Delta t) = \bar{n}_{j,k} - \lambda \left(H^{x,(1)}_{j+(1/2),k} - H^{x,(1)}_{j-(1/2),k} \right) - \mu \left(H^{y,(1)}_{j,k+(1/2)} - H^{y,(1)}_{j,k-(1/2)} \right)$$
$$+ \Delta t \left[\frac{\bar{n}_{j+1,k} - 2\bar{n}_{j,k} + \bar{n}_{j-1,k}}{(\Delta x)^2} + \frac{\bar{n}_{j,k+1} - 2\bar{n}_{j,k} + \bar{n}_{j,k-1}}{(\Delta y)^2} \right], \qquad \text{(A 28)}$$

where $\lambda := \Delta t / \Delta x$, $\mu := \Delta t / \Delta y$, and, as before, the dependence of all terms on the right-hand side of (A 28) on t is suppressed to simplify the notation. Our goal is to show that if all $\bar{n}_{j,k}(t)$ are non-negative, then all $\bar{n}_{j,k}(t + \Delta t)$ will also be non-negative.

Since

$$H^{x,(1)}_{j+(1/2),k} = a^{(1)}_{j+(1/2),k} \left(\frac{1 + \text{sign}(a^{(1)}_{j+(1/2),k})}{2} n^E_{j,k} + \frac{1 - \text{sign}(a^{(1)}_{j+(1/2),k})}{2} n^W_{j+1,k} \right) \quad \text{(A 29)}$$

and

$$H^{y,(1)}_{j+(1/2),k} = b^{(1)}_{j,k+(1/2)} \left(\frac{1 + \text{sign}(b^{(1)}_{j,k+(1/2)})}{2} n^N_{j,k} + \frac{1 - \text{sign}(b^{(1)}_{j,k+(1/2)})}{2} n^S_{j,k+1} \right), \quad \text{(A 30)}$$

and since by the conservation property of the piecewise-linear reconstruction (A 16) the identity

$$\bar{n}_{j,k} = \tfrac{1}{8} \left(n^E_{j,k} + n^W_{j,k} + n^N_{j,k} + n^S_{j,k} \right) + \tfrac{1}{2}\bar{n}_{j,k} \qquad \text{(A 31)}$$

is true, we obtain:

$$\bar{n}_{j,k}(t + \Delta t) = \left[\frac{1}{8} + \lambda a^{(1)}_{j-(1/2),k} \frac{1 - \text{sign}(a^{(1)}_{j-(1/2),k})}{2} \right] n^W_{j,k}$$
$$+ \left[\frac{1}{8} - \lambda a^{(1)}_{j+(1/2),k} \frac{1 + \text{sign}(a^{(1)}_{j+(1/2),k})}{2} \right] n^E_{j,k}$$
$$- \lambda a^{(1)}_{j+(1/2),k} \frac{1 - \text{sign}(a^{(1)}_{j+(1/2),k})}{2} n^W_{j+1,k}$$
$$+ \lambda a^{(1)}_{j-(1/2),k} \frac{1 + \text{sign}(a^{(1)}_{j-(1/2),k})}{2} n^E_{j-1,k}$$
$$+ \left[\frac{1}{8} + \mu b^{(1)}_{j,k-(1/2)} \frac{1 - \text{sign}(b^{(1)}_{j,k-(1/2)})}{2} \right] n^S_{j,k}$$

$$+ \left[\frac{1}{8} - \mu b^{(1)}_{j,k+(1/2)} \frac{1 + \text{sign}(b^{(1)}_{j,k+(1/2)})}{2} \right] n^N_{j,k}$$

$$- \mu b^{(1)}_{j,k+(1/2)} \frac{1 - \text{sign}(b^{(1)}_{j,k+(1/2)})}{2} n^S_{j,k+1}$$

$$+ \mu b^{(1)}_{j,k-(1/2)} \frac{1 + \text{sign}(b^{(1)}_{j,k-(1/2)})}{2} n^N_{j,k-1}$$

$$+ \bar{n}_{j,k} \left[\frac{1}{2} - \Delta t \left(\frac{2}{(\Delta x)^2} + \frac{2}{(\Delta y)^2} \right) \right]$$

$$+ \Delta t \left[\frac{\bar{n}_{j+1,k} + \bar{n}_{j-1,k}}{(\Delta x)^2} + \frac{\bar{n}_{j,k+1} + \bar{n}_{j,k-1}}{(\Delta y)^2} \right]. \tag{A 32}$$

This means that the new values $\{\bar{n}_{j,k}(t + \Delta t)\}$, computed using (A 32), are linear combinations of the non-negative cell averages $\{\bar{n}_{j,k}\}$ and the reconstructed point value $\{n^E_{j,k}, n^W_{j,k}, n^N_{j,k}, n^S_{j,k}\}$, which are also non-negative provided the reconstruction is performed using (A 18) and (A 19), as explained above. These linear combinations will be convex combinations provided the following CFL condition is satisfied:

$$\Delta t \leqslant \min \left\{ \frac{\Delta x}{8 \max_{j,k} \left\{ |a^{(1)}_{j+(1/2),k}| \right\}}, \frac{\Delta y}{8 \max_{j,k} \left\{ |b^{(1)}_{j,k+(1/2)}| \right\}}, \frac{(\Delta x)^2 (\Delta y)^2}{4((\Delta x)^2 + (\Delta y)^2)} \right\}. \tag{A 33}$$

This condition thus guarantees positivity of $\{\bar{n}_{j,k}(t + \Delta t)\}$.

A.2. *Centred-difference scheme for the vorticity equation*

We now describe a semi-discrete second-order finite-difference scheme for the vorticity equation (A 3). We approximate all derivatives in (A 3) using the centred differences and evolve the point values of vorticity at the corners of the finite-volume cells by solving the following system of time-dependent ODEs:

$$\frac{d}{dt} \omega_{j+(1/2),k+(1/2)} = -u_{j+(1/2),k+(1/2)} \frac{\omega_{j+(3/2),k+(1/2)} - \omega_{j-(1/2),k+(1/2)}}{2\Delta x}$$

$$- v_{j+(1/2),k+(1/2)} \frac{\omega_{j+(1/2),k+(3/2)} - \omega_{j+(1/2),k-(1/2)}}{2\Delta y}$$

$$+ Sc \left[\frac{\omega_{j+(3/2),k+(1/2)} - 2\omega_{j+(1/2),k+(1/2)} + \omega_{j-(1/2),k+(1/2)}}{(\Delta x)^2} \right.$$

$$\left. + \frac{\omega_{j+(1/2),k+(3/2)} - 2\omega_{j+(1/2),k+(1/2)} + \omega_{j+(1/2),k-(1/2)}}{(\Delta y)^2} \right]$$

$$- \gamma Sc (n_x)_{j+(1/2),k+(1/2)}, \tag{A 34}$$

using the same ODE solver which was used to solve system equation (A 10). In (A 34), we have $\omega_{j+(1/2),k+(1/2)}(t) \approx \omega(x_{j+(1/2)}, y_{k+(1/2)}, t)$, the velocities $u_{j+(1/2),k+(1/2)}$ and $v_{j+(1/2),k+(1/2)}$ are defined in (A 36) below and $(n_x)_{j+(1/2),k+(1/2)}$ is computed by the centred-difference formula

$$(n_x)_{j+(1/2),k+(1/2)} = \frac{(n^N_{j+1,k} + n^S_{j+1,k+1}) - (n^N_{j,k} + n^S_{j,k+1})}{2\Delta x}. \tag{A 35}$$

Notice that both $n^N_{j,k}$ and $n^S_{j,k+1}$ are second-order approximations of $n(x_j, y_{k+(1/2)})$.

A.3. *Velocities*

Once the point values of the vorticity $\{\omega_{j+(1/2),k+(1/2)}\}$ are evolved, we solve the elliptic equation (A 4) to obtain the point values of the stream-function at the same set of points, $\{\psi_{j+(1/2),k+(1/2)}\}$, from which the velocities u and v can be easily computed using the following centred-difference approximations:

$$\left.\begin{aligned} u_{j+(1/2),k+(1/2)} &= \frac{\psi_{j+(1/2),k+(3/2)} - \psi_{j+(1/2),k-(1/2)}}{2\Delta y}, \\ v_{j+(1/2),k+(1/2)} &= -\frac{\psi_{j+(3/2),k+(1/2)} - \psi_{j-(1/2),k+(1/2)}}{2\Delta x}, \end{aligned}\right\} \quad (A\,36)$$

$$\left.\begin{aligned} u_{j+(1/2),k} &= \frac{\psi_{j+(1/2),k+(1/2)} - \psi_{j+(1/2),k-(1/2)}}{\Delta y}, \\ v_{j,k+(1/2)} &= -\frac{\psi_{j+(1/2),k+(1/2)} - \psi_{j-(1/2),k+(1/2)}}{\Delta x}. \end{aligned}\right\} \quad (A\,37)$$

A.4. *Numerical boundary conditions*

We split the boundary $\partial\Omega$ into a top part, $\partial\Omega_{top} = \{(x,y) \mid -a \leqslant x \leqslant a, \ y = d\}$, a bottom part, $\partial\Omega_{bot} = \{(x,y) \mid -a \leqslant x \leqslant a, \ y = 0\}$, and two sides, $\partial\Omega_{side} = \{(x,y) \mid x = \pm a, \ 0 \leqslant y \leqslant d\}$. We cover the computational domain Ω with a Cartesian grid consisting of $j_{max} \times k_{max}$ uniform cells.

The boundary conditions at the top $\partial\Omega_{top}$ model a fluid–air surface preventing cell flux and providing full oxygen saturation (see Metcalfe & Pedley 2001; Tuval *et al.* 2005). More precisely, we implement (2.10) in the following way (for n and c the ghost cell technique is used):

$$\left.\begin{aligned} \bar{n}_{j,k_{max}+1} &:= \bar{n}_{j,k_{max}} e^{\alpha(1-\bar{c}_{j,k_{max}})}, \quad \bar{c}_{j,k_{max}+1} = 1, \\ \omega_{j+(1/2),k_{max}+(1/2)} &= \psi_{j+(1/2),k_{max}+(1/2)} = 0, \quad \forall j, \end{aligned}\right\} \quad (A\,38)$$

where the boundary condition for n is obtained from the first formula in (2.10) by taking into account the fact that at the top $c \sim 1$ and thus $r(c) = 1$ and by integrating $(\ln n)_y = \alpha c_y$ with respect to y from $y_{k_{max}}$ to $y_{k_{max}+1}$.

The boundary conditions on $\partial\Omega_{bot}$ model a solid bottom preventing cell and oxygen fluxes. More precisely, we implement (2.11) as follows (the ghost cell technique is now used for n, c and ψ):

$$\left.\begin{aligned} \bar{n}_{j,0} &:= \bar{n}_{j,1}, \quad \bar{c}_{j,0} = \bar{c}_{j,1}, \quad \omega_{j+(1/2),(1/2)} = -2\frac{\psi_{j+(1/2),(3/2)} - \psi_{j+(1/2),(1/2)}}{(\Delta y)^2}, \\ \psi_{j+(1/2),-(1/2)} &= \psi_{j+(1/2),(3/2)}, \quad \forall j. \end{aligned}\right\} \quad (A\,39)$$

For details on stream-function and vorticity boundary conditions we refer the reader to Thom (1933), see also the review paper E & Liu (1996).

Finally, the two sides $\partial\Omega_{side}$ are connected with periodic boundary conditions.

A.5. *Time integration*

Finally, to obtain a fully discrete scheme, the system equation (A 10), (A 34) should be solved by a stable ODE solver of an appropriate order. Since this system is rather stiff, one may prefer to use an implicit or large-stability-domain explicit ODE solver (see the discussion in the beginning of § 3). However, this may affect the positivity-preserving property of the resulting fully discrete scheme. In Chertock & Kurganov (2008) and Chertock *et al.* (2010), we have shown that if one uses a strong-stability-preserving (SSP) method (either a Runge–Kutta or a multistep one) or an IMEX-SSP
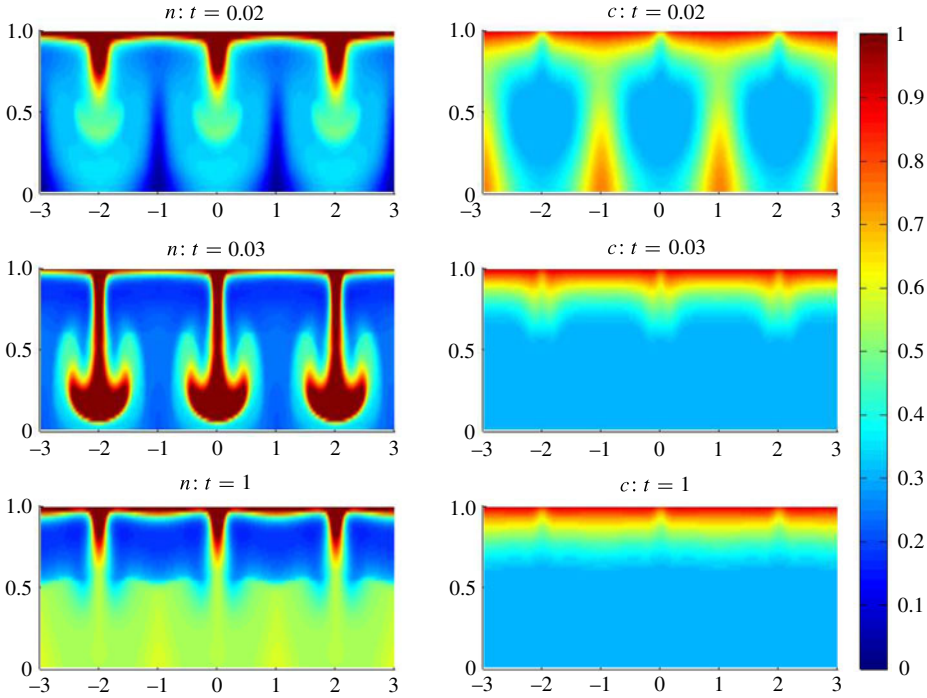
FIGURE 18. Solution (the n- and c-components) of (2.3)–(2.6), (7.1) with $\beta = 10^2$, $\gamma = 10^4$. Moreover, for c below c^*, the diffusion coefficient for n switches from D_n to $D_n/10$.

or a positivity-preserving IMEX method together with the aforementioned adaptive strategy, then the positivity of n will be ensured.

Appendix B. Additional computations

Comparing figures 18 and 15 shows that the solution almost stays the same when diminishing the diffusion coefficient for n from D_n to $D_n/10$ for c below c^*. The same calculations have been done when the diffusion coefficient for n switches from D_n to $D_n/5$, $D_n/50$ and $D_n/100$. To increase readability and limit the length of the article, they are not shown. They give evidence that the numerical scheme is able to treat these cases. Moreover, for $D_n/100$, we observe relatively sharp edges which seem unphysical.

REFERENCES

BUSSE, F. H. 1985 Transition to turbulence in Rayleigh–Bénard convection. In *Hydrodynamic Instabilities and the Transition to Turbulence*, *Topics in Applied Physics*, vol. 45. pp. 97–137. Springer.

BUSSE, F. H. & SIEBER, M. 1991 Regular and chaotic patterns of Rayleigh–Bénard convection. In *Bifurcation and Chaos: Analysis, Algorithms, Applications (Würzburg, 1990)*, *International Series of Numerical Mathematics*, vol. 97. pp. 79–92. Birkhäuser.

CARRILLO, J. A. & MOLL, J. S. 2009 Numerical simulation of diffusive and aggregation phenomena in nonlinear continuity equations by evolving diffeomorphisms. *SIAM J. Sci. Comput.* **31** (6), 4305–4329.

CHANDRASEKHAR, S. 1981 *Hydrodynamic and Hydromagnetic Stability*. Dover.

CHAPMAN, C. J. & PROCTOR, M. R. E. 1980 Nonlinear Rayleigh–Bénard convection between poorly conducting boundaries. *J. Fluid Mech.* **101** (4), 759–782.

CHERTOCK, A. & KURGANOV, A. 2008 A positivity preserving central-upwind scheme for chemotaxis and haptotaxis models. *Numer. Math.* **111**, 169–205.

CHERTOCK, A., KURGANOV, A., WANG, X. & WU, Y. 2010 On a chemotaxis model with saturated chemotactic flux. *Kinet. Relat. Models* **5**, 51–95.

COOK, A. W. & DIMOTAKI, P. E. 2001 Transition stages of Rayleigh–Taylor instability between miscible fluids. *J. Fluid Mech.* **443**, 69–99.

DI FRANCESCO, M., LORZ, A. & MARKOWICH, P. 2010 Chemotaxis–fluid coupled model for swimming bacteria with nonlinear diffusion: global existence and asymptotic behaviour. *Discrete Contin. Dyn. Syst.* A **28** (4), 1437–1453.

DOLAK, Y. & SCHMEISER, C. 2005 The Keller–Segel model with logistic sensitivity function and small diffusivity. *SIAM J. Appl. Maths* **66** (1), 286–308(electronic).

DOMBROWSKI, C., CISNEROS, L., CHATKAEW, S., GOLDSTEIN, R. & KESSLER, J. 2004 Self-concentration and large-scale coherence in bacterial dynamics. *Phys. Rev. Lett.* **93**, 098103.

DUAN, R.-J., LORZ, A. & MARKOWICH, P. 2010 Global solutions to the coupled chemotaxis-fluid equations. *Commun. Part. Diff. Equ.* **35**, 1–39.

E, W. & LIU, J.-G. 1996 Vorticity boundary condition and related issues for finite difference schemes. *J. Comput. Phys.* **124**, 368–382.

FELLNER, K. & RAOUL, G. 2010 Stable stationary states of non-local interaction equations. *Math. Models Meth. Appl. Sci.* **20** (12), 2267–2291.

FILBET, F. 2006 A finite volume scheme for the Patlak–Keller–Segel chemotaxis model. *Numer. Math.* **104** (4), 457–488.

GHORAI, S. & HILL, N. A. 1999 Development and stability of gyrotactic plumes in bioconvection. *J. Fluid Mech.* **400**, 1–31.

GHORAI, S. & HILL, N. A. 2002 Axisymmetric bioconvection in a cylinder. *J. Theor. Biol.* **219** (2), 137–152.

GOTTLIEB, S., SHU, C.-W. & TADMOR, E. 2001 Strong stability-preserving high-order time discretization methods. *SIAM Rev.* **43**, 89–112.

HAŠKOVEC, J. & SCHMEISER, C. 2009 Stochastic particle approximation for measure valued solutions of the 2D Keller–Segel system. *J. Stat. Phys.* **135** (1), 133–151.

HERNANDEZ-ORTIZ, J. P., UNDERHILL, P. T. & GRAHAM, M. D. 2009 Dynamics of confined suspensions of swimming particles. *J. Phys.: Condens. Matter* **21**, 204107.

HIGUERAS, I. & ROLDÁN, T. 2006 Positivity-preserving and entropy-decaying IMEX methods. In *Ninth International Conference Zaragoza-Pau on Applied Mathematics and Statistics*, *Monografías del Seminario Matemático ''García de Galdeano''*, vol. 33. pp. 129–136, Prensas Univ. Zaragoza, Zaragoza.

HILL, N. A. & PEDLEY, T. J. 2005 Bioconvection. *Fluid Dyn. Res.* **37**, 1–20.

HILLESDON, A. J. & PEDLEY, T. J. 1996 Bioconvection in suspensions of oxytactic bacteria: linear theory. *J. Fluid Mech.* **324**, 223–259.

HILLESDON, A. J., PEDLEY, T. J. & KESSLER, O. 1995 The development of concentration gradients in a suspension of chemotactic bacteria. *Bull. Math. Biol.* **57**, 299–344.

HOPKINS, M. & FAUCI, L. 2002 A computational model of the collective fluid dynamics of motile micro-organisms. *J. Fluid Mech.* **455**, 149–174.

LEVEQUE, R. 2002 *Finite Volume Methods for Hyperbolic Problems*. Cambridge University Press.

LIE, K.-A. & NOELLE, S. 2003 On the artificial compression method for second-order nonoscillatory central difference schemes for systems of conservation laws. *SIAM J. Sci. Comput.* **24**, 1157–1174.

LORZ, A. 2010 Coupled chemotaxis fluid model. *Math. Models Meth. Appl. Sci.* **20**, 1–17.

MEDOVIKOV, A. A. 1998*a* DUMKA3 code available at http://dumkaland.org/.

MEDOVIKOV, A. A. 1998*b* High order explicit methods for parabolic equations. *BIT* **38**, 372–390.

METCALFE, A. M. & PEDLEY, T. J. 1998 Bacterial bioconvection: weakly nonlinear theory for pattern selection. *J. Fluid Mech.* **370**, 249–270.

METCALFE, A. M. & PEDLEY, T. J. 2001 Falling plumes in bacterial bioconvection. *J. Fluid Mech.* **445**, 121–149.

NESSYAHU, H. & TADMOR, E. 1990 Nonoscillatory central differencing for hyperbolic conservation laws. *J. Comput. Phys.* **87**, 408–463.

PARESCHI, L. & RUSSO, G. 2005 Implicit–explicit Runge–Kutta schemes and applications to hyperbolic systems with relaxation. *J. Sci. Comput.* **25** (1–2), 129–155.

SAINTILLAN, D. & SHELLEY, M. J. 2007 Orientational order and instabilities in suspensions of self-locomoting rods. *Phys. Rev. Lett.* **99**, 058102.

SHARP, D. 1984 An overview of Rayleigh–Taylor instability. *Physica* D **12**, 3–18.

SWEBY, P. 1984 High resolution schemes using flux limiters for hyperbolic conservation laws. *SIAM J. Numer. Anal.* **21**, 995–1011.

THOM, A. 1933 The flow past circular cylinders at low speeds. *Proc. R. Soc. Lond.* A **141**, 651–669.

TUVAL, I., CISNEROS, L., DOMBROWSKI, C., WOLGEMUTH, C., KESSLER, J. & GOLDSTEIN, R. 2005 Bacterial swimming and oxygen transport near contact lines. *Proc. Natl Acad. Sci.* **102**, 2277–2282.

WOLGEMUTH, C. W. 2008 Collective swimming and the dynamics of bacterial turbulence. *Biophys. J.* **95** (4), 1564–1574.